Icarus 306 (2018) 225–242

Contents lists available at ScienceDirect

Icarus

journal homepage: www.elsevier.com/locate/icarus

How old are lunar lobate scarps? 1. Seismic resetting of crater size-frequency distributions

Carolyn H. van der Bogert[a,*], Jaclyn D. Clark[a], Harald Hiesinger[a], Maria E. Banks[b,c,d], Thomas R. Watters[b], Mark S. Robinson[e]

[a] Institut für Planetologie, Westfälische Wilhelms-Universität Münster, Wilhelm-Klemm-Str. 10, 48149 Münster, Germany
[b] Center for Earth and Planetary Studies of the National Air and Space Museum, Smithsonian Institution, Washington, DC 20560, USA
[c] Planetary Science Institute, Tucson, AZ 85719, USA
[d] NASA Goddard Space Flight Center, Greenbelt, MD 20771, USA
[e] School of Earth and Space Exploration, Arizona State University, Tempe, AZ 85287, USA

ARTICLE INFO

Article history:
Received 5 September 2017
Revised 19 December 2017
Accepted 18 January 2018
Available online 2 February 2018

Keywords:
Lobate scarp
Crater size-frequency distributions
Moon
Absolute model ages
Seismic shaking

ABSTRACT

Previous studies have estimated the ages of lunar lobate scarps, some of the youngest tectonic landforms on the Moon, based on the estimated life-times of their fresh morphologies and associated small graben, using crater degradation ages, or via buffered and traditional crater size-frequency distribution (CSFD) measurements. Here, we reexamine five scarps previously dated by Binder and Gunga (1985) with crater degradation ages to benchmark the evaluation of both the buffered and traditional CSFD approaches for determination of absolute model ages (AMAs) at scarps. Both CSFD methods yield similar ages for each individual scarp, indicating that fault activity not only can be measured on the scarp itself, but also in the surrounding terrain – an indication that tectonic activity causes surface renewal both adjacent to and even kilometers distant from scarps. Size-frequency variations in the regions surrounding the scarps are thus useful for studying the extent and severity of the ground motion caused by coseismic slip events during scarp formation. All age determination approaches continue to indicate that lunar lobate scarps were active in the late Copernican, with some scarps possibly experiencing activity within the last 100 Ma.

1. Introduction and background

The relatively fresh appearance of lunar lobate scarps, including their sharp morphology, undegraded appearance, and the absence of large (> 400 m) superposed craters, indicates that they are very young (Fig. 1, Lucchitta, 1976; Schultz, 1976; Binder and Gunga, 1985; Watters et al., 2010; 2012, 2015). Using Apollo panoramic photographs, Binder and Gunga (1985) derived age estimates for 21 scarps using crater degradation measurements on craters transected by or superposed on the scarps. The craters were classified according to their degradation state using calibration data from Moore et al. (1980) and Boyce and Moore (1980) using the method of Trask (1971), which was developed from techniques proposed by Pohn and Offield (1970) and Offield and Pohn (1970). A maximum age for each scarp was determined from craters crosscut by the scarp, while a minimum age was drawn from craters crosscutting the scarp. Thus, the method of Binder and Gunga (1985) yielded a range of ages that they interpreted to bracket the formation age of the scarps. Most scarps gave relatively well-defined formation ages indicative of a very short formation period, while a few scarps seem to have experienced extended and/or multiple episodes of deformation. The age estimates of the scarps range from 60 ± 30 Ma to 680 ± 250 Ma with uncertainties of + 2× to −4×, indicating that lunar scarps are Copernican in age (Binder and Gunga, 1985). Factors that may bias the age estimates to be older than actual include: (1) the resolution (~2 m) of the panoramic images which results in the softening of rims of small (10–40 m) craters making them appear larger and older, and (2) different degradational characteristics of the terrain than the flat mare surfaces that Trask (1971) used to calibrate the technique. For example, several scarps measured have significant slopes, so the superposed craters likely degrade faster and appear older due to gravity-driven mass wasting than similar craters on flat mare surfaces, thus giving older apparent ages (Binder and Gunga, 1985). As

* Corresponding author.
E-mail addresses: vanderbogert@uni-muenster.de (C.H. van der Bogert), j.clark@uni-muenster.de (J.D. Clark), hiesinger@uni-muenster.de (H. Hiesinger), maria.e.banks@nasa.gov (M.E. Banks), watterst@si.edu (T.R. Watters), robinson@ser.asu.edu (M.S. Robinson).

https://doi.org/10.1016/j.icarus.2018.01.019

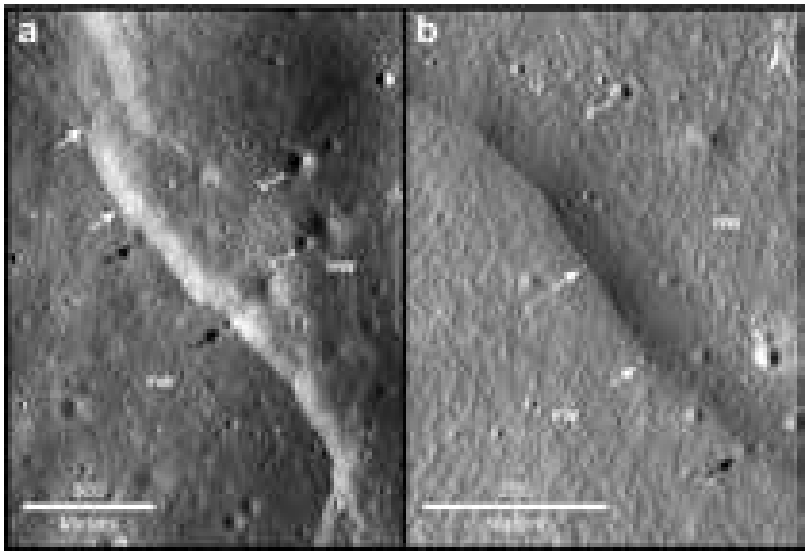

Fig. 1. Morphology of lunar lobate scarps, where HW = hanging wall, FW = footwall, and V = highly degraded craters with shallow v-shaped floors. White arrows indicate craters superposing the scarp, whereas black arrows show craters that are crosscut by the scarp. (a) A sharp fault trace crosscutting older small craters, along with smaller superposing fresh craters, attest the relative youth of the Mandel'shtam-3 scarp. (b) Areas proximal to the scarps, particularly if the local slopes are > 15°, often exhibit a small-scale hummocky texture with subdued v-shaped craters, for example at Henderson-2 scarp.

Table 1
Investigated scarps, their locations, and key parameters for the data used in this study. (The scarps are named provisionally after the crater within which they occur or after nearby large craters.).

Scarp	Latitude (°)	Longitude (°)	NAC image(s)	Pixel scale (m/pixel)	Incidence angle (°)
Henderson-2	7.77	152.07	M115319317	1.16	72
			M1159101897	1.19	55
Kondratyuk	−15.03	116.78	M119088861	1.15	65
Koval'skiy-3	20.90	102.60	M1184149045	0.91	64
Mandel'shtam-3	5.83	161.03	M103460280	1.22	64
Morozov	6.54	129.94	M1113318442	1.23	52
			M180322716	1.26	77

such, the true ages of the lobate scarps are assumed to be younger than the apparent ages calculated by Binder and Gunga (1985).

The Lunar Reconnaissance Orbiter Camera (LROC; Robinson et al., 2010) provides new coverage of previously known scarps, including some measured by Binder and Gunga (1985), as well thousands of newly discovered scarps (Watters et al., 2010, 2015; Banks et al., 2012; Clark et al., 2017a). Since the study by Binder and Gunga (1985), the method of crater size-frequency distribution (CSFD) measurement was also developed to determine absolute model ages for geological units across the Moon using a lunar crater chronology calibrated to the radiometric and exposure ages of samples collected at Apollo and Luna landing sites (Hartmann, 1966; Crater Analysis Techniques Working Group, 1979; Neukum, 1983; Neukum et al., 2001; Hiesinger et al., 2011). Here, we evaluate the usefulness of CSFD measurements for determining absolute model ages (AMAs) for scarp formation. The new data and more advanced techniques allow a renewed investigation of "how old are lunar lobate scarps?"

Traditional CSFD measurements are used to derive ages for geologically distinct units, such as mare basalt flows and impact deposits, whereas buffered crater counting (BCC) methods were developed for assessing the ages of linear structural features, based on the model age represented by craters crosscutting the features (Tanaka, 1982; Wichman and Schultz, 1989; Kneissl et al., 2015). Here, we investigate the use of both methods for dating lobate scarps. We present both types of measurements for five scarps (Fig. 2, Table 1) that were also investigated by Binder and Gunga (1985), so that we can use ages determined via a different technique to benchmark our results. Five of the 21 scarps studied by Binder and Gunga (1985) have complete or almost complete image coverage at the incidence angles required for CSFD measurements in addition to DTM products. We also discuss the findings of Senthil Kumar et al. (2016), who used the BCC technique to date four scarps in Schrödinger Basin, in the context of our results.

2. Methods and data

The measurement of CSFDs relies on the selection of appropriate count areas. The criteria include selection of an area with low slopes, because slopes can affect the rate at which craters degrade due to gravity-driven mass wasting, and thus their apparent age (Basilevsky, 1976; Meyer et al., 2016). The area should also contain no obvious secondary craters (herringbone patterns, clusters, chains), and should represent one geological unit, based on compositional and morphological analysis (e.g., Neukum, 1983; Hiesinger et al., 2011 and references therein). The proper selection of count areas and the measurement of CSFDs for the derivation of AMAs is described in detail by e.g., Hartmann (1966), Crater Analysis Techniques Working Group (1979), Neukum (1983), Hiesinger et al., (2000) and Michael and Neukum (2010). The image data should have similar or identical solar incidence angles for studies comparing areas in different image frames or products, because differences in incidence angles affect the population of craters visible for measurement (Soderblom, 1970; Young, 1975; Wilcox et al., 2005; Ostrach et al., 2011). Ostrach et al. (2011) recommend using incidence angles of 60–80°.

To derive the relative or absolute age of a photogeological unit, one must (1) measure the surface area of the unit and (2) measure the rim diameters of each primary impact crater within the unit. All craters within the count areas are included, regardless of mor-

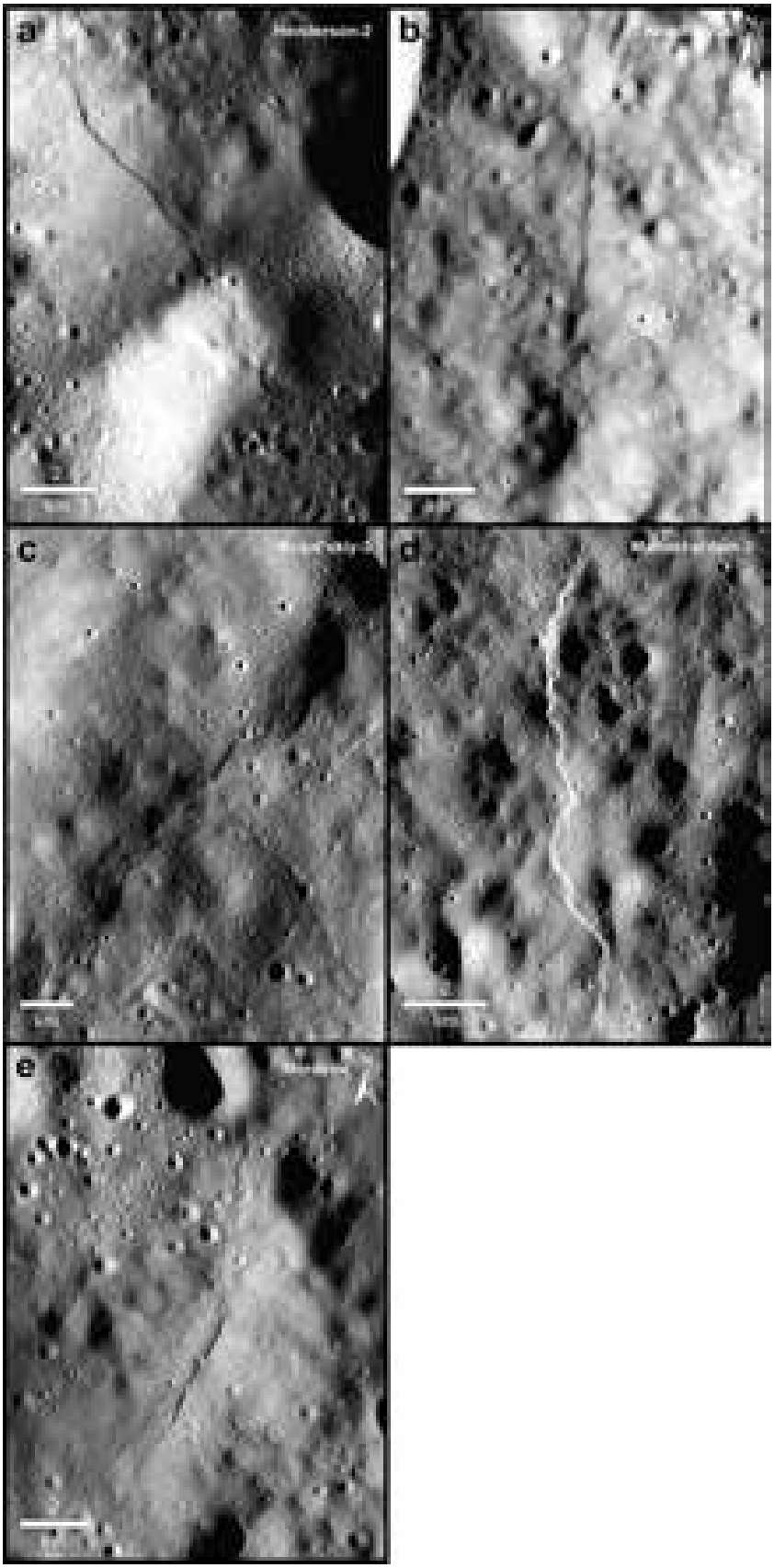

Fig. 2. Overviews of the scarps dated by Binder and Gunga (1985), which we reinvestigated using CSFD methods (Table 1) as imaged by the SELENE Terrain Camera. (a) Henderson-2, (b) Kondratyuk, (c) Koval'skiy-3, (d) Mandel'shtam-3, and (e) Morozov.

Table 2
Absolute model ages (AMAs) using Poisson age determination (PDF) and cumulative fits (CumF) of lunar lobate scarps derived using the standard technique in this study. Values in parentheses are derived exclusively on the basis of the R-plot, as discussed in the text. CSFDs exhibiting equilibrium are indicated by 'na', because they cannot be fit with an AMA.

Scarp	Count area (km^2)	Fit range (m)	PDF (Ma)	$N(1)$ ($\times10^{-5}$)	CumF (Ma)	$N(1)$ ($\times10^{-5}$)
Henderson-2						
HW	0.661	20–500	110 ± 20	8.87	95 ± 20	7.93
Face	0.255	10–100	77 ± 9	6.47	71 ± 8	5.93
FW	0.874	na	na	na	na	na
Kondratyuk						
HW	0.935	10–1000	79 ± 5	6.58	75 ± 4	6.23
FW	0.989	25–1000	58^{+20}_{-10}	4.90	56 ± 20	4.71
Koval'skiy-3						
HW	0.710	20–1000	150 ± 20	12.3	170 ± 20	13.9
FW	0.638	20–35	160 ± 30	13.8	170 ± 20	14.1
		60–1000	$1000\ ^{+400}_{-300}$	8.64	1100 ± 400	9.24
Mandel'shtam-3						
FWD(a)	0.393	10–28	(120 ± 9)	(10.4)	(130 ± 9)	(11.1)
FWP(a)	0.393	10–20	(160 ± 10)	(13.3)	(170 ± 9)	(14.1)
HWP(a)	0.393	10–22	110 ± 9	9.53	120 ± 9	10.3
HWD(a)	0.393	na	na	na	na	na
FWD(b)	0.393	10–25	67 ± 7[a]	5.60	67 ± 7	5.61
		25–300	$190\ ^{+50}_{-40}$	15.9	200 ± 50	17.0
FWP(b)	0.393	10–35	89 ± 8	7.47	110 ± 9	9.55
		33–800	$350\ ^{+100}_{-90}$	29.6	360 ± 100	30.4
HWP(b)	0.393	10–38	98 ± 8	8.23	100 ± 8	8.53
HWD(b)	0.393	10–38	(75 ± 7)	(6.25)	(80 ± 7)	(6.74)
FWD(c)	0.393	25–65	320 ± 100	26.7	310 ± 100	25.6
FWP(c)	0.393	10–35	120 ± 9	10.2	120 ± 9	10.8
		40–800	320 ± 60	26.5	320 ± 60	26.9
HWP(c)	0.393	10–100	93 ± 8	7.77	99 ± 8	8.30
HWD(c)	0.393	10–40	130 ± 9	11.2	150 ± 10	12.5
		48–72	$1000\ ^{+400}_{-300}$	85.6	920 ± 300	76.8
Morozov[b]						
HW(a)	0.513	na	na	na	na	na
HW(b)	0.513	13–1000	84 ± 10	7.02	81 ± 9	6.79
FW	0.513	na	na	na	na	na

[a] May reflect the age of a small young crater within this area.
[b] HW(a) corresponds to Morozov-1, whereas HW(b) and FW represent Morozov-2 (see Section 3.5).

phology, except obvious secondary and endogenic craters. The cumulative crater density of a geologic unit is related to the time the unit has been exposed to the meteorite flux, giving a relative age for the unit. Here, we report the cumulative crater density using a 1 km reference diameter, expressed as $N(1)$. Radiometric and/or exposure ages from returned lunar samples were correlated with crater retention ages at the sample collection sites and coupled with empirical measurements of the lunar production function, allowing the development of a lunar chronology curve that is used to derive AMAs for geologic units across the Moon (e.g., Neukum, 1983; Neukum and Ivanov, 1994; Neukum et al., 2001; Stöffler and Ryder, 2001; Stöffler et al., 2006; Le Feuvre and Wieczorek, 2011).

The traditional approach for defining count areas requires the selection of a single geologic unit forming a representative surface for the measurement of the CSFD. In contrast, a buffered crater counting (BCC) technique was developed for determining ages for linear features independently from the surrounding geologic units (Tanaka, 1982; Wichman and Schultz, 1989; Fassett and Head, 2008; Kneissl et al., 2015). The technique uses craters (as well as ejecta, if desired) that superpose the linear feature to derive an AMA. Buffer areas are calculated from the diameter of each crosscutting crater and a crater frequency is derived separately for each crater and its respective buffer area. For linear features, only craters that are observed to crosscut the feature are included in the measurement (Tanaka, 1982; Wichman and Schultz, 1989). For features with a definable width, such as valleys, the area of the feature is defined as W_v, and is added to the half-width of the buffer extending from the middle of the feature for each crater diameter D, so that $S_{buffer} = aD + 0.5W_v$, where a is equal to 1 when considering only crosscutting crater rims and is equal to 1.5 when considering overlapping ejecta blankets (Fassett and Head, 2008). For their study of mercurian scarps, Giacomini et al. (2015) used both the stringent linear method, as well as defining an area W_v as encompassing the scarp antiform. Senthil Kumar et al. (2016) also used the scarp antiform area for their lunar scarp measurements. We defined the scarp trace as an area with almost negligible width, and only included craters that crosscut that scarp trace. Senthil Kumar et al. (2016) and we both exclude the consideration of crater ejecta.

For CSFD measurements and morphological observations at the studied lobate scarps (Fig. 2), we used the LROC Narrow Angle Camera (NAC) (Robinson et al., 2010) images listed in Table 1, as well as NAC-DTM (Digital Terrain Model) derived slope maps (Tran et al., 2010; Henriksen et al., 2017) or slope maps generated from the LOLA-SELENE Terrain Camera DEM (Digital Elevation Model) (Barker et al., 2016; Haruyama et al., 2008). The images were calibrated and map-projected using the Integrated Software for Imagers and Spectrometers (ISIS) software package (Anderson et al., 2004) and imported into Esri's ArcGIS software package, where we used CraterTools (Kneissl et al., 2011, 2015) to perform crater size-frequency distribution measurements. Using Craterstats (Michael and Neukum, 2010), the CSFDs were plotted in cumulative and relative (R-plot) forms using pseudo-log binning. AMAs were fit both (1) in cumulative form with pseudo-log binning (18 bins/decade) and a cumulative resurfacing correction, where applicable (Table 2), and (2) using Poisson timing analysis of the unbinned datasets (Table 2; Michael and Neukum, 2010; Michael, 2013; Michael et al., 2012, 2016). (Poisson timing analysis cannot currently be applied to BCC datasets. BCC data sets are thus fit using the standard cumulative plot.) Fit ranges were determined

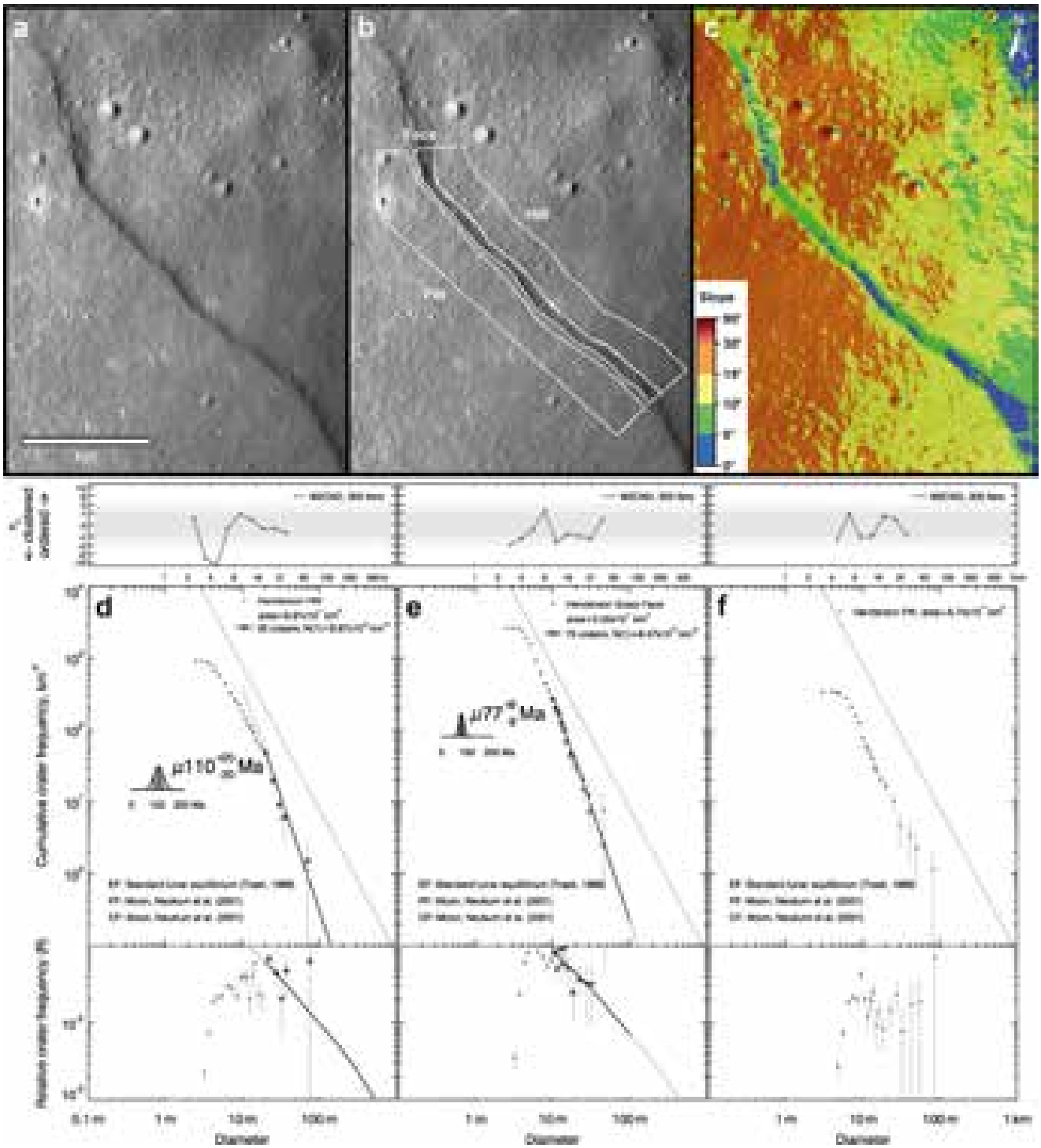

Fig. 3. Henderson-2 scarp (a) NAC frame M115319317, (b) count area locations, where HW = hanging wall, FW = footwall, and Face = scarp face, and (c) NAC DTM-derived slope map. (d–f) Cumulative and relative crater frequency plots showing absolute model ages (AMAs) determined using Poisson timing analysis, where applicable. (d) The headwall exhibits an age of ~110 Ma, (e) while the scarp face is ~77 Ma. (f) The footwall cannot be fit with an age, because the CSFD is in equilibrium. Randomness analyses (top panels) show no evidence for unidentified secondaries in the CSFDs, except for ~3–4 m craters in the HW area – diameters which were not used to fit the AMA.

with the aid of the R-plots, which provide more detail for particular crater size bins than the cumulative plot. Randomness analysis was used to determine whether the collected data sets contained unidentified secondary craters that would be expressed as clusters of craters within different size bins (Michael et al., 2012). We used the crater-size standard distribution or production function (PF) and chronology function (CF) of Neukum et al. (2001), which is valid for craters with diameters > 10 m and < 100 km.

Using the standard CSFD measurement approach, we defined count areas at the scarps on a case by case basis to investigate the crater populations at and near the scarps. The count areas were selected to encompass relatively flat surfaces and to avoid craters that exhibit morphologies such as herringbone, clustering, and non-circular rims that indicate they may be secondaries (Neukum, 1983). Using this approach, we investigate the potential effects of shaking on the removal of small craters on and sur-

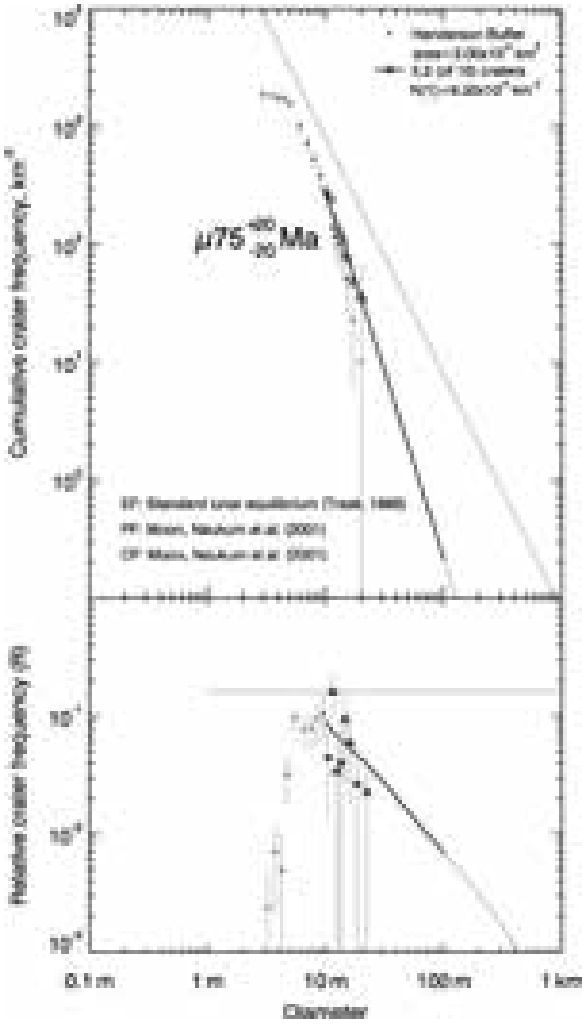

Fig. 4. The absolute model age (AMA) derived for Henderson-2 via buffered CSFD measurements (cumulative fit) is similar to those derived for the traditional count area on the scarp face (Fig. 3e) and overlaps the error bars of the headwall measurement.

rounding the scarps. We compare these traditional results with BCC measurements for each of five scarps previously investigated by Binder and Gunga (1985): Henderson-2, Kondratyuk, Koval'skiy-3, Mandel'shtam-3, and Morozov (Table 1, Fig. 2). (The scarps are named provisionally after the crater within which they occur or after nearby large craters.)

3. Results

3.1. Henderson

The Henderson lobate scarp complex consists of four scarp segments in and to the west of Henderson B crater. Henderson-2 scarp (7.77°N, 152.07°E), as identified by Binder and Gunga (1985), is located west-northwest of Henderson B crater along the southwest wall of an unnamed highly degraded ~200 km diameter crater. The ~21 km long scarp crosscuts the degraded crater rims of two ancient craters (Figs. 2a and 3a). The northern portion, which has a fault plane dipping to the NE, is 4.87 km long, has a linear appearance, and is uphill-facing along the crater wall. Banks et al. (2012) determined that this section of the scarp has a relief of at least 14 m and a scarp face slope of 12° based on profiles derived from individual LOLA tracks. The southern portion of the scarp transects the rims of the unnamed crater and another crater immediately adjacent to the south. The scarp then runs to the east before disappearing about 9 km west of Henderson B. A ~7 km long scarp segment (Henderson-1) is also visible along the southwest wall of Henderson B crater itself.

We selected traditional count areas along and on the scarp face (Fig. 3b). The count area that best meets the selection criteria is the face of the scarp, which exhibits slopes of < 10° in the NAC-DTM slope map (Fig. 3c). The slopes are generally lower than the value reported by Banks et al. (2012), likely due to the spatial limitations of the LOLA profiles used in their study. Two count areas adjacent to the scarp face were selected on the head and footwalls. However, these areas have slopes of up to 30°, which may affect the derived ages. Due to the presence of small clusters of secondaries, the limited NAC coverage at incidence angles required for CSFD measurements, and to the even steeper slopes of the surrounding crater wall, we did not select areas more distal to the scarp for investigation. The buffered CSFD count area was defined along the same portion of the scarp trace as the traditional count areas.

The CSFD derived from the hanging wall (HW) gives an AMA of 110 Ma ± 20 Ma, when fit using Poisson timing analysis (Fig. 3d). (See Table 2 for all cumulative fits using the resurfacing correction, where applicable.) The level scarp face provides a somewhat younger AMA of 77 ± 9 Ma (Fig. 3e), which agrees well with the age derived via the BCC method (75 ± 20 Ma, Fig. 4). An AMA could not be derived for the footwall (FW) (Fig. 3f), because the distribution runs parallel to the standard equilibrium line of Trask (1966), and thus cannot be fit with the production function of Neukum et al. (2001).

The surfaces adjacent to the scarp have a hummocky morphology that makes it difficult to identify small craters. On the hanging wall, the three largest craters in the count area (> 37 m) have highly degraded rims, with a v-shaped profile (in NAC-DTMs), that suggest they may have been present prior to the occurrence of the crater chronometer resetting event. However, their exclusion from the age analysis does not alter the results. The craters on the scarp face have a somewhat sharper morphology. On the footwall, 10 of 11 craters larger than 22 m in diameter exhibit highly degraded rims, which makes it difficult in most cases to reliably determine their diameters.

The hanging wall exhibits some clustering of craters at diameters of ~3–4 m, as seen in the randomness analysis (Fig. 3d, top panel), which are likely to be secondary craters. Indeed, chains and clusters of small secondaries are visible in the northern section of the HW counting area. However, these craters are smaller than the range used for the age fit. There is no evidence for secondary contamination on the scarp face or footwall (Fig. 3e, f).

3.2. Kondratyuk

Kondratyuk (15.27°S, 116.77°E) is an uphill-facing, slightly arcuate, ~22 km long lobate scarp that crosses the floor of Kondratyuk crater from north to south along the base of its eastern crater wall (Fig. 2b; Banks et al., 2012). We focused on a section of the scarp centered at 15.03°S, 116.78°E (Fig. 5a). Two narrow count areas adjacent to the scarp were selected due to the limited NAC image coverage, which ends just east of the scarp (Fig. 5b). The hanging wall count area exhibits lower slopes (0–5°) than the footwall count area (10–15°) (Fig. 5c). Due to the spatially limited NAC coverage at incidence angles required for CSFD measurements, and to the steeper slopes of the surrounding crater wall, we did not select areas more distal to the scarp for investigation.

The hanging wall at Kondratyuk exhibits an AMA of 79 ± 5 Ma (Fig. 5d, Table 2). Some of the largest craters (> 45 m in diameter) in the HW count area exhibit high levels of degradation, in particular subdued crater rims. One large crater in the northern part of

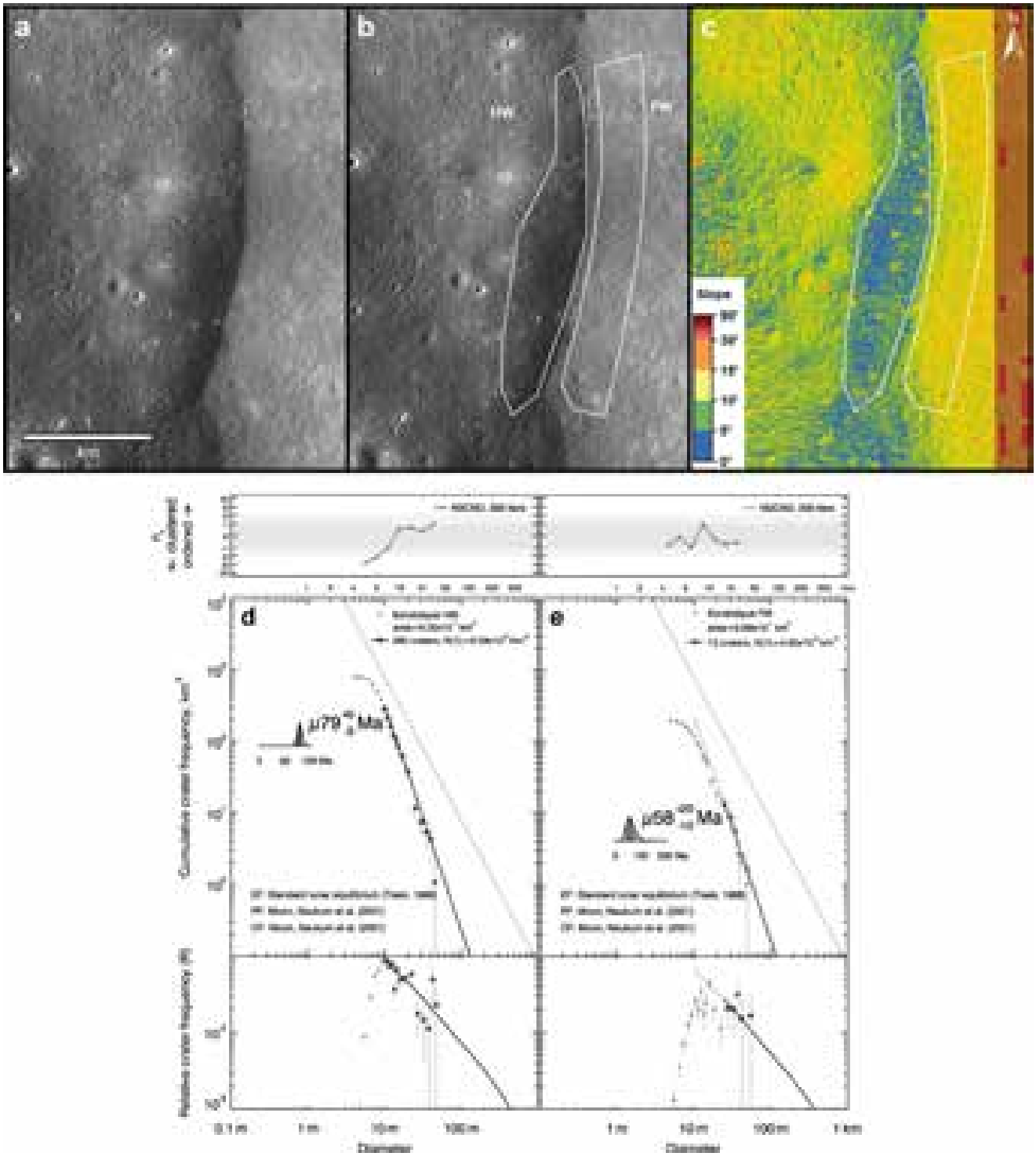

Fig. 5. Kondratyuk scarp (a) NAC frame M119088861, (b) count area locations, where HW = hanging wall and FW = footwall, and (c) NAC DTM-derived slope map with LOLA-SELENE Terrain Camera DEM-derived slope basemap. (d,e) Cumulative and relative crater frequency plots showing AMAs determined using Poisson timing analysis. (d) The headwall yields an AMA of ~77 Ma, and the footwall (e) an AMA of ~58 Ma. The headwall exhibits possible secondary craters at diameters up to ~8 m (d, top panel), but not at diameters used to fit model ages.

the count area was so degraded that it was not possible to define a rim. However, more of the largest craters have relatively sharp rims compared with those at Henderson. The texture of the hanging wall surface is somewhat hummocky, although less so than at Henderson where the slopes were greater (up to 30° versus 0–5°). The footwall is hummockier than the hanging wall possibly due to the greater slope on the footwall, making it difficult to see craters less than about 10 m in diameter, while the larger craters exhibit more extreme degradation than those on the hanging wall. The level of degradation makes it difficult to accurately measure the diameters of the largest craters. The texture and degradation level of the footwall cause the CSFD to reflect a younger surface age (58^{+20}_{-10} Ma; Fig. 5e) than the headwall. For Kondratyuk, the BCC AMA (63 ± 20 Ma, Fig. 6) is closest in value to that of the footwall,

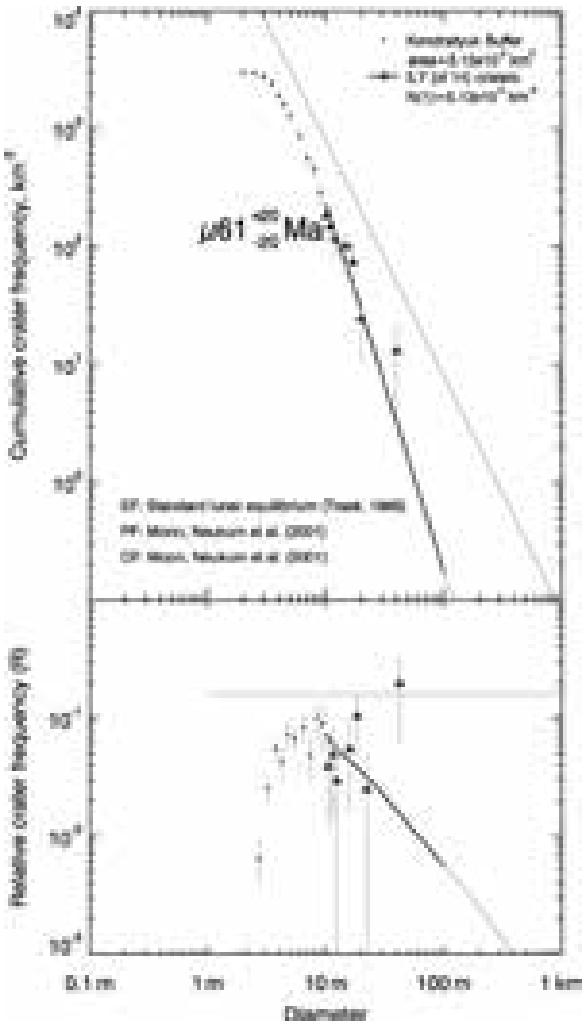

Fig. 6. The AMA derived for Kondratyuk via buffered CSFD measurements (cumulative fit) is similar to that derived for the traditional count area on the footwall, but younger than that of the headwall.

but all the AMAs are within error of the BCC value. It is possible that the BCC value was pushed lower by the accumulation of slope debris along the scarp trace, which could have erased craters that post-dated the scarp formation.

The randomness analyses for each of the traditional CSFDs (Fig. 5d, e) do not show significant secondary contamination of the count areas, except for craters < ~8 m in diameter on the hanging wall. This size range is smaller than that used to fit model ages.

3.3. Koval'skiy-3

Koval'skiy-3 scarp (20.90°S, 102.60°E), as defined by Binder and Gunga (1985), is located between Koval'skiy B and Koval'skiy D craters, approximately 30 km northeast of the Koval'skiy crater rim (Fig. 2c). The ~14 km long arcuate scarp traverses northeast over slightly hummocky terrain (Fig. 7a). A smaller ~3 km-length scarp (Koval'skiy-4) is located 5 km west of the southern tip of the main larger scarp, and exhibits a flat and more linear appearance. Scarp segments 1 and 2 are located to the north, but are not yet imaged by LROC NAC.

We selected a count area roughly in the middle of the longer scarp segment (20.96°S, 102.54°E), where the influence of slumping and secondary craters is limited and the slopes are the shallowest (Fig. 7b, c). (There is a fresh crater at the northeastern terminus of the scarp segment that we avoided.) The hanging wall can be fit with an AMA of 150 ± 20 Ma (Fig. 7d), while the footwall exhibits an AMA of 160 ± 30 Ma (Fig. 7e). Here, the slight differences in slope between the two count areas do not appear to greatly affect the age determination. Neither CSFD appears to be affected by secondary contamination. The footwall also shows an additional age of ~1 Ga for craters larger than 60 m in diameter (Fig. 7e). These craters exhibit more degraded crater rims than the smaller craters, and do not exhibit a v-shaped morphology or hummocky texture. However, ~200 m diameter craters to the northeast on the footwall do show these morphologies. Craters smaller than 15 m in diameter in the count areas have a shallower CSFD, consistent with a population in equilibrium. Given that the CSFDs at Henderson-2 and Kondratyuk do not exhibit small crater populations that are in equilibrium, the crater equilibrium at Koval'skiy-3 is consistent with an older formation age, as also reflected in the AMAs.

We attempted to define a buffered area along the scarp trace. However, the segmented and discontinuous scarp is hard to easily define close-up at NAC resolution, although a NAC-derived DTM might allow for improvement. Nevertheless, for the sake of comparison, we defined a set of count lines along the white dotted line denoting the scarp in Fig. 7a, which gave an AMA of 75 ± 20 Ma (Fig. 8a). Because this age is much less than that determined from the traditional count areas, we also determined a BCC age for only the southern segment, which lies between the two traditional count areas. The resulting age of 120 ± 50 Ma is more similar to the traditional AMAs (Fig. 8b). Closer examination reveals that the northern segment of the scarp is missing craters in some of the larger crater diameter bins, perhaps due to the 15–30° slopes in that area. Thus, we do not consider the combined age to be robust.

3.4. Mandel'shtam

Mandel'shtam (S3) (Binder and Gunga, 1985) or Mandel'shtam-3 (Banks et al., 2012) (6.83°N, 161.03°E) is a long scarp with 20 subscarps, located in the middle of the extensive Mandel'shtam scarp complex (Fig. 2d). The ~12 km long segment 3 lies within relatively flat terrain, with an easterly fault dip direction (Fig. 9a). Because this segment lies in the middle of the NAC image pair and is one of the longest lunar lobate scarps in this study, we were able to examine three rows of CSFD measurements to explore the variation of AMAs along the trace of and with distance from the fault. Count areas were placed close to the scarp trace and then ~3–3.5 km away, distal from the scarp on both the head and footwalls (Fig. 9b).

The northernmost count areas give ages of 160 ± 10 Ma and 110 ± 9 Ma on the proximal footwall FWP(a) and headwall HWP(a), respectively. The distal footwall FWD(a) yields an age of 120 ± 9 Ma, while the distal headwall HWD(a) is in equilibrium, so that an age cannot be fit (Fig. 10a–d, Table 2). All of the ages derived from the footwall areas in the northern transect could only be fit on the basis of the R-plots (bottom panels, Fig. 10a,b), because the amount of resetting of the CSFD was minimal enough that it does not appear in the cumulative representation of the data. However, the R-plot can be used to determine the range of crater diameters that can be fit with a young isochron. In these cases, the cumulative resurfacing correction is needed to visualize the fit on the cumulative plots.

The central count areas give ages ranging from 67 ± 7 Ma to 98 ± 8 Ma, with some areas showing older ages (190^{+50}_{-40} and 350^{+100}_{-90} Ma) recorded at the larger crater diameters – see the respective fit ranges in Table 2 (Fig. 10e–h). HWD(b) exhibits an age of 75 ± 7 Ma, which was fit exclusively using the R-plot, as described above. The youngest age (67 ± 7 Ma), at FWD(b), may result from the occurrence of a fresh 72 m diameter crater in that area that likely affects the smaller crater population directly surround-

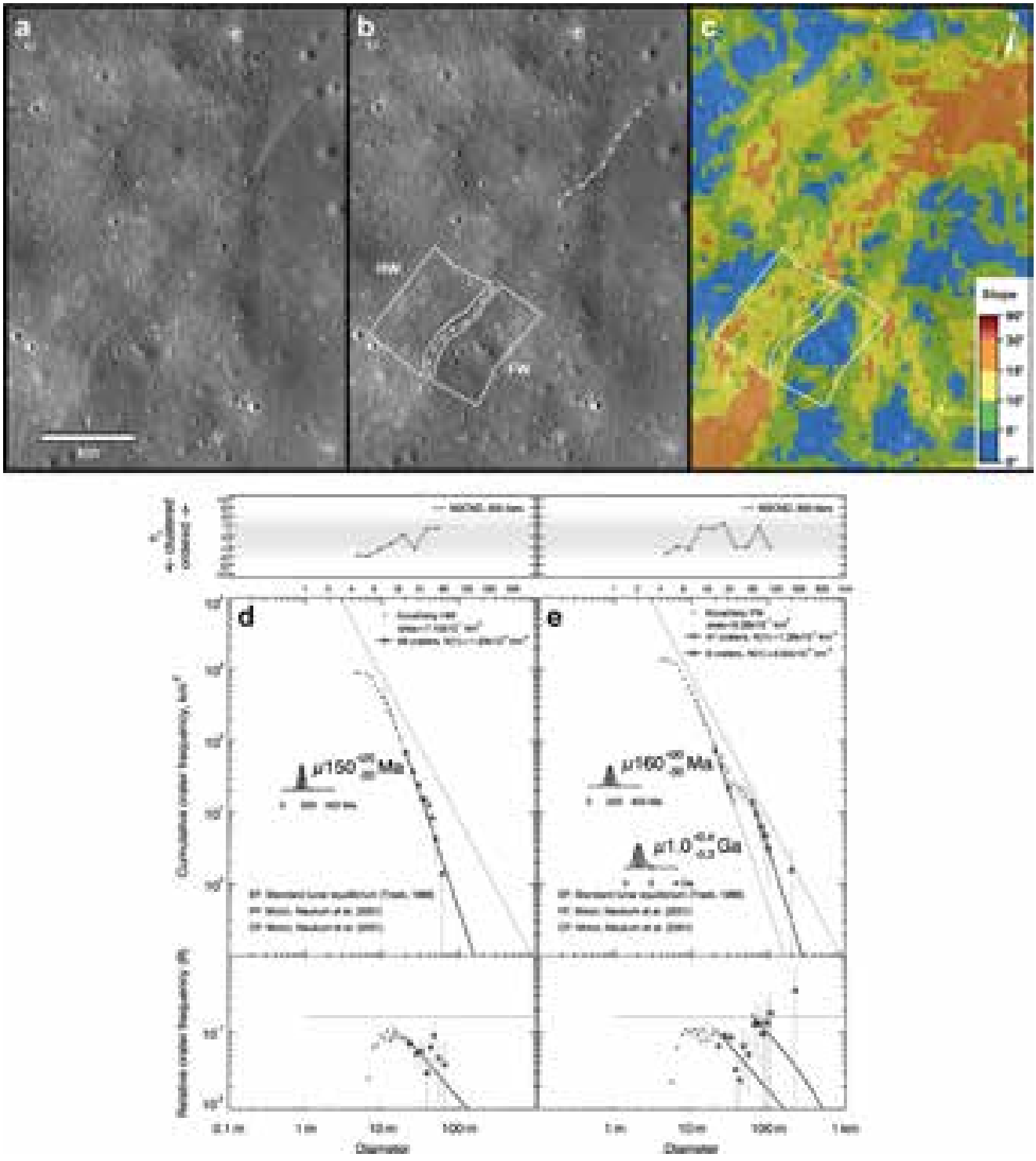

Fig. 7. Koval'skiy-3 scarp (a) NAC frame M1184149045, (b) count area locations and scarp trace (white dotted line), where HW = hanging wall and FW = footwall, and (c) LOLA-SELENE Terrain Camera DEM-derived slope map overlay. (d,e) Cumulative and relative crater frequency plots showing AMAs determined using Poisson timing analysis. (d) The headwall gives an age of ~150 Ma. (e) The footwall shows an age of ~160 Ma, but also exhibits an older age of ~1 Ga.

ing it. Thus, we eliminate this age determination from our further scarp-age analysis.

The southernmost count areas give ages of 93 ± 8 Ma to 130 ± 9 Ma, with some areas again showing older ages of about 320 Ma (Fig. 10i–l, Table 2). The HWD(c) area shows the oldest age of all the investigated areas for craters 48–72 m in diameter of about 1 Ga. In summary, the investigated areas give a group of ages from ~90–160 Ma, and a second group of ages from ~320–350 Ma. The BCC-derived AMA (56 ± 8 Ma, Fig. 11) is significantly younger than the traditionally derived ages. This could either indicate a problem with our measurement, or it could indicate that Mandel'shtam-3 experienced additional creep after the events recorded on the foot- and head walls.

Craters > 50 m in diameter exhibit highly degraded rims and a v-shaped profile with wedge-shaped shadows, as do many of the craters with diameters of ~20–50 m (e.g., HWP(b), Fig. 1a,

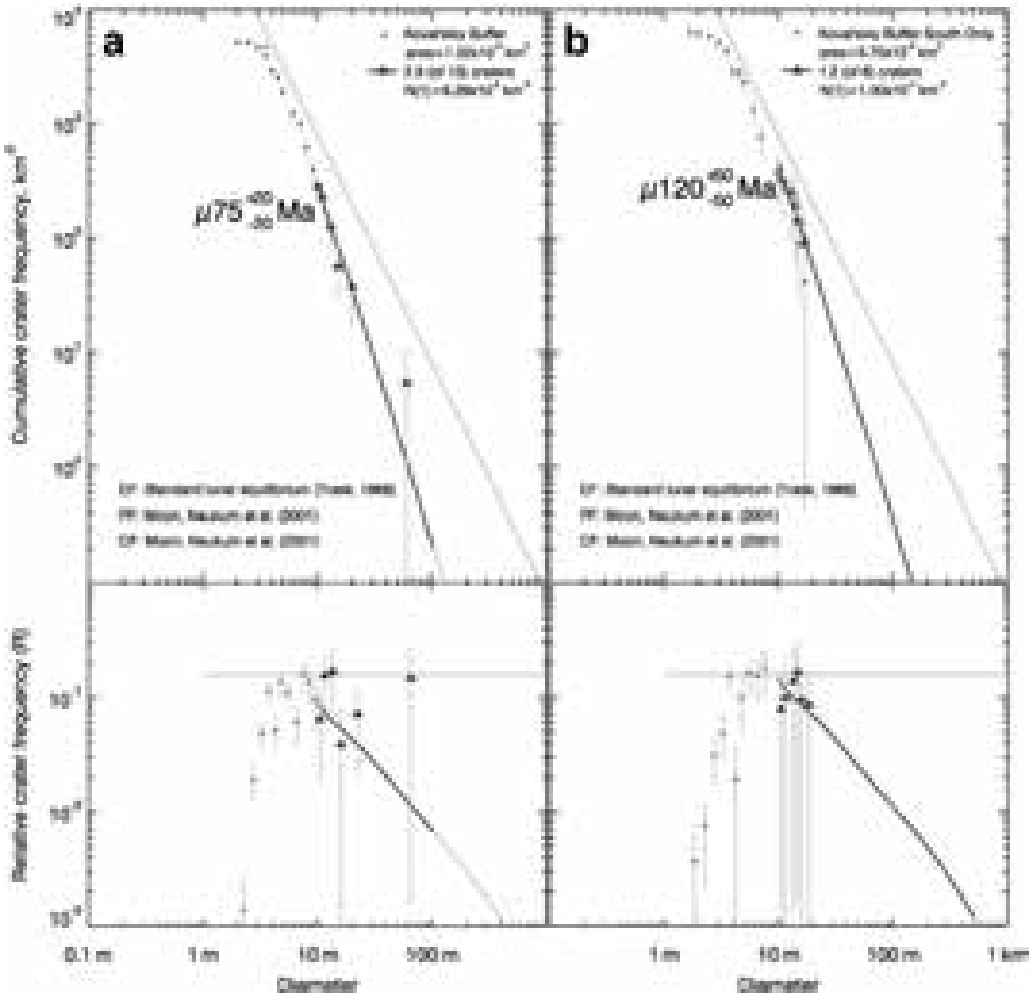

Fig. 8. AMAs derived for Koval'skiy-3 via buffered CSFD measurements (cumulative fits). (a) AMA derived from both scarp segments illustrated in Fig. 7b. (b) AMA from the southern scarp segment between the traditional count areas. The age derived from the southern segment is more consistent with the ages of the traditional count areas. The younger age displayed by the combined areas may result from poor statistics and/or the steep slopes at the northern segment.

Fig. 9d,e), corresponding to the diameter range where a cumulative resurfacing correction is required for the CSFD in the cumulative plot (e.g., Fig. 10g). The steeper slopes in the southern portion of the count area may cause slightly fewer craters to be observed either due to their faster degradation or the more pronounced hummocky texture of the surface that makes it harder to distinguish small crater rims (see Fig. 9e,f). When evaluating the range of crater diameters affected by the crater chronometer resetting event, we can look at the range of diameters fit for each count area (Table 2). Those locations with a wider range of reset crater diameters (e.g., HWP(c) with a fit range of 10–100 m, in contrast with FWP(a) with a fit range of 10–20 m) experienced a more significant resetting event than areas with smaller affected diameter ranges.

3.5. Morozov

Morozov (6.54°N, 129.94°E), about 340 km east of Mendeleev crater, consists of two main segments spanning a distance of ~12 km (Fig. 2e). The longest scarp in this area is Morozov-1 with a length of 4.94 km, whereas Morozov-2 is located to the north (6.77°N, 130.00°E) and is 3.03 km long (Banks et al., 2012). Morozov is uphill-facing, with the southern segment following the wall of a depression that is likely an ancient impact crater. Morozov-2 runs up the ancient crater wall to the north. We selected count areas adjacent to Morozov-2 and in the transfer region between it and Morozov-1, because the slopes adjacent to Morozov-1 tend to exceed 15° (Fig. 12a–c). The southernmost hanging wall count area, HW(a), gives an AMA of 84 ± 10 Ma, whereas the second hanging wall area in the north, HW(b), cannot be fit with an AMA, because it appears to be in equilibrium (Fig. 12d). The footwall also cannot be fit with an AMA (Fig. 12e), because the CSFD does not conform to the lunar production function, rather it appears to be in equilibrium. The two northerly count areas exhibit a hummocky texture, with highly degraded craters of all sizes, whereas the southerly hanging wall area is smoother with more fresher small craters (> 13 m diameter) observable.

Morozov does not currently have NAC coverage with illumination from the east. As a result, it is not possible to define a good buffered CSFD measurement line along the foot of the scarp face, which is in shadow. Thus, we used the SELENE Terrain Camera orthomap (Haruyama et al., 2008) to generate a BCC measurement (Fig. 13). Despite the fact that the data set only contains 7 craters, the result of 91 ± 30 Ma is within its error to the age measured on HW(b). The absence of a fit on the R-plot, however, argues against the robustness of this fit. The slightly older BCC age could result from the likelihood that the crater diameters were all measured slightly larger than actual due to the lower resolution of the SELENE data (7 m/pixel) versus the NAC frames. All the craters measured were less than 5 pixels across, which means that their diam-

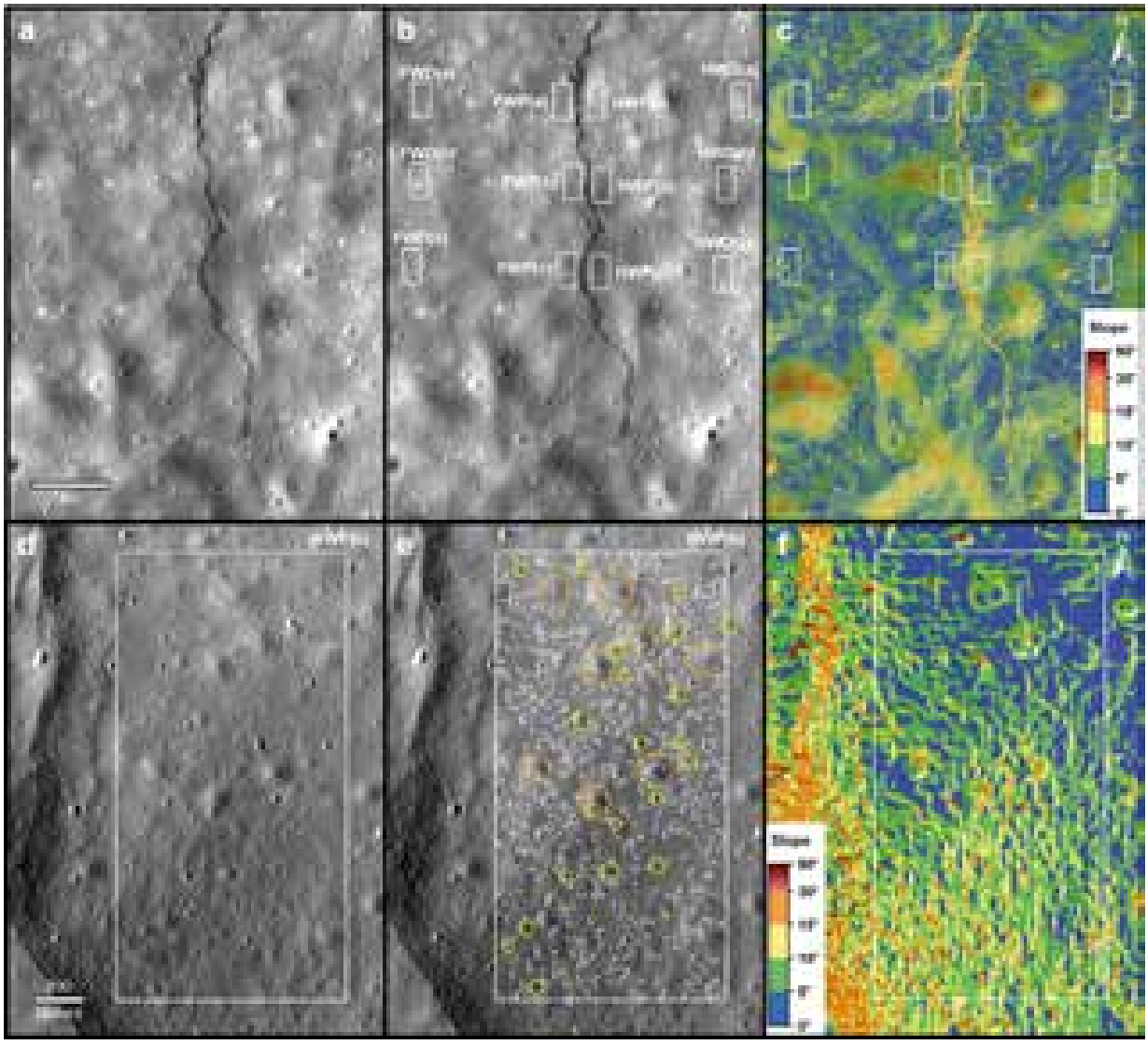

Fig. 9. Mandel'shtam-3 scarp (a) NAC frame M191909925, (b) count area locations, where HW = hanging wall, FW = footwall, D = distal, and P = proximal, and (c) NAC DTM-derived slope map. (d) Count area HWP(b) shows the effects of both scarp-related and slope-facilitated degradation (see Discussion). (e) Craters > 50 m in diameter exhibit highly degraded rims and a funnel-shape (orange), while many craters with diameters of ~20–50 m show these morphologies (yellow). (f) The steeper slopes in the southern portion of the count area are associated with a slightly lower crater frequency than the rest of the count area. (For interpretation of the references to color in this figure legend, the reader is referred to the web version of this article.)

eters could not be robustly measured, because the crater rims can no longer be clearly resolved.

4. Discussion

4.1. Selection of count areas in challenging terrain

The selection of count areas adjacent to scarps can encounter challenges that cause a decrease in the precision of the age determinations. First, image coverage of small features such as scarps has greatly improved due to the work of recent and ongoing missions, such as SELENE and LRO. However, even at this writing all lobate scarps do not have complete coverage at the illumination conditions required for CSFD measurements. For example, the east-facing scarp face of Morozov has not yet been imaged with the NAC with illumination from the east. As a result, we used the lower resolution SELENE Terrain Camera orthomap. In addition, due to spacecraft and mission constraints, only select scarps have stereo-imaging, such that NAC-derived DTMs could be generated. Thus, it was not yet possible to obtain NAC stereo for all the studied scarps. However, the LOLA-SELENE Terrain Camera-derived slope map provides regional information in the case of Koval'skiy.

Regional to local slope maps are useful for helping select count areas that are as flat as possible. Steep slopes contribute particularly to degradation of small craters and affect the local level of geometric saturation equilibrium that can be expressed in the CSFD (Basilevsky, 1976; Schultz et al., 1977; Mahanti et al., 2018). In particular, Basilevsky (1976) notes that crater lifetime is an inverse exponential function of slope steepness. While we were able to select count areas adjacent to or on the faces of the scarps with minimal regional slopes in many cases, steep slopes may have stymied our ability to produce ideal count areas in some cases. At Henderson-2, the hanging and footwalls both exhibit slopes > 10° The footwall did not provide a CSFD that could be fit with an age, while the hanging wall provided an age ~35 Ma older than the scarp

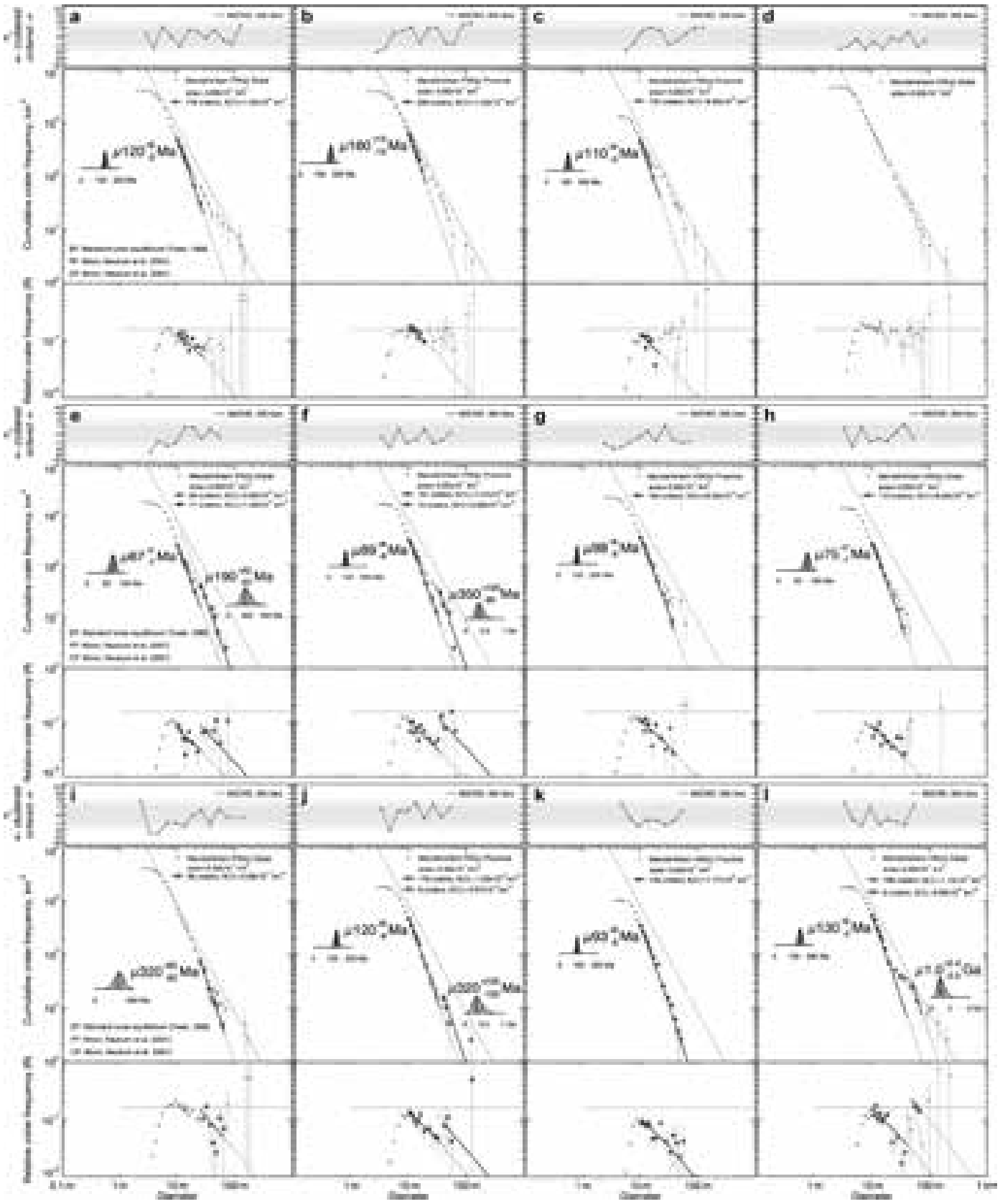

Fig. 10. Cumulative and relative crater frequency plots showing AMAs determined using Poisson timing analysis for Mandel'shtam-3, which are organized to correspond with the geographic locations of the measurement areas on the footwall and headwall in Fig. 9. (a) Footwall FW(a) distal, (b) FW(a) proximal, (c) Headwall HW(a) proximal, (d) HW(a) distal; (e) FW(b) distal, where a fresh 80 m diameter crater is likely responsible for the ~67 Ma AMA, (f) FW(b) proximal, (g) HW(b) proximal, (h) HW(b) distal; (i) FW(c) distal, (j) FW(c) proximal, (k) HW(c) proximal and (l) HW(c) distal areas.

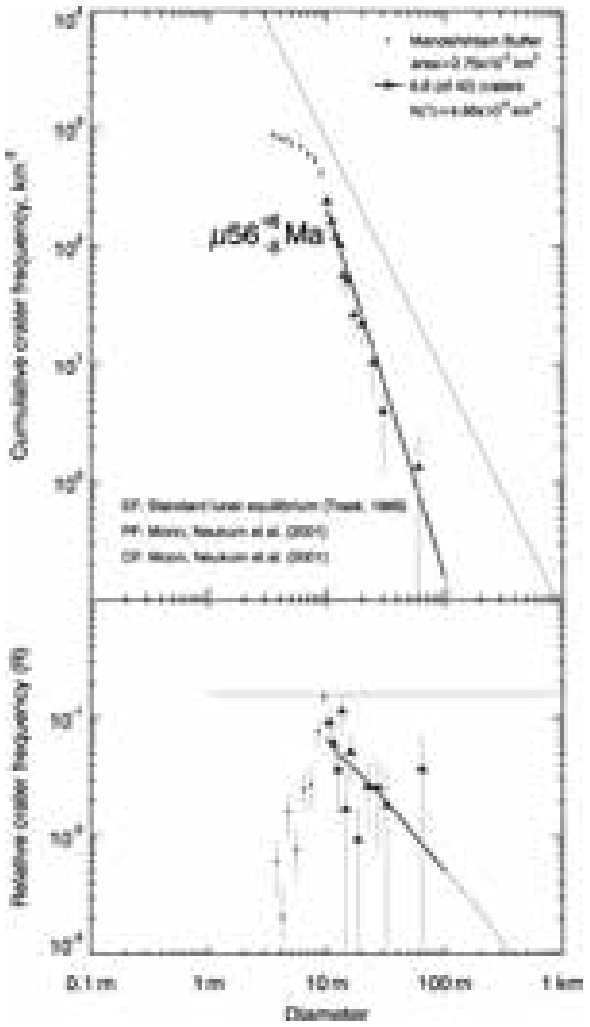

Fig. 11. The AMA derived for Mandel'shtam-3 via buffered CSFD measurements (cumulative fit) is less than those derived for the traditional count areas around the scarp.

face count area with slopes < 10° (Fig. 3). However, at Kondratyuk, the footwall count area (> 10° slope) gave an age ~20 Ma younger than the hanging wall (primarily slopes < 5°, Fig. 5). At Koval'skiy, both traditional counting areas have slopes of < 15° and give ages that are similar within error (Fig. 7). However, the presence of 15–30° slopes along the northern scarp segment may be partially responsible for the much younger age derived from the combined BCC measurement versus the age fit to just the southern scarp segment (which is consistent with the traditional AMAs). Given that it is unclear how great of an effect steep slopes may have on derivation of robust AMAs, it is best to select count areas with shallow to no slopes to mitigate the effect of slope on the CSFDs.

Some count areas may necessarily be rather small due the small sizes of some scarps, as well as limitations due to the locally steep slopes. Smaller count areas provide less robust statistics, but even in consideration of the errors introduced, useful age estimates can be derived (Pasckert et al., 2015; van der Bogert et al., 2015; Williams et al., 2017). Using the 100 m/pixel LROC WAC mosaic, Pasckert et al. (2015) showed that 4 km^2 areas within a larger 100 km^2 area reasonably reproduce the age derived from that larger area, but have lower accuracy. To eliminate the effects of subsequent geological activity that could locally reset the CSFDs, van der Bogert et al. (2015) modeled randomly generated CSFDs for differently aged surfaces to investigate the statistical effects on fitting of AMAs to increasingly small count areas, and found the accuracy and precision of AMAs decrease with decreasing count area size. For example, for count areas with sizes between 0.25 and 1 km^2 on a surface with an age of 100 Ma, the errors generated by the count area size would be 20–30%. As a result, the variation mentioned in the previous paragraph between count areas with different slopes could also reflect the natural variation between the small count area sizes. Buffered CSFD measurements are particularly sensitive to count area size constraints due to their definition along the often small, thin scarps. Count area size effects are caused by the reduced number of craters available to measure in smaller areas, in addition to variations in the random distribution of the craters, which may exhibit clusters or even sparse regions with no craters (van der Bogert et al., 2015). In particular, the Possion analysis technique is useful for CSFDs with small numbers of craters (and even for analysis of an area with no craters), because this method evaluates the probability that a surface of a particular age would exhibit the population of craters (or absence of craters) (Michael et al., 2016; Williams et al., 2017). As such, we applied Poisson analysis to our traditional CSFD measurements. However, it cannot currently be applied to buffered CSFDs. Regardless of the uncertainties involved, the age information that we can derive from the lobate scarps is consistent with recent geological activity.

4.2. Comparison of buffered and traditional CSFD measurements

The BCC technique has been used to derive AMAs for large structural features across the Solar System (e.g., Wichman and Schultz, 1989; Basilevsky et al., 2011; Giacomini et al., 2015; Kneissl et al., 2015; Fegan et al., 2017), but the technique has been only recently applied to a small number of lunar lobate scarps (e.g., Senthil Kumar et al., 2016; Clark et al., 2017b), and has not yet been applied to small scarps recently discovered on Mercury (Watters et al., 2016). Large-scale scarps on Mercury are many 10s to 100s of kilometers long, and most have been found to be much older than lunar scarps (Banks et al., 2015; Giacomini et al., 2015). Thus lobate scarps on Mercury both crosscut and are crosscut by significant numbers of craters larger than 10 m in diameter. This allows the straightforward determination of AMAs, since the chronology function is defined for craters down to 10 m in diameter. In contrast, many lunar lobate scarps are only a few to tens of kilometers in length, have small relief compared to their mercurian counterparts, and are crosscut by few craters larger than 10 m in diameter (e.g., Watters et al., 2010; Banks et al., 2012; Williams et al., 2013; Roggon et al., 2017). The approach used by Senthil Kumar et al. (2016) included all the craters that were present within the area defined by the scarp antiform width, which was then buffered using the craters crosscutting this area. Increasing the area of the measurement allows the improvement of the statistics and reduction of the overall error bars. However, we chose to apply the strict approach, which only considers craters that directly crosscut the scarps, because we wanted to only measure craters that unequivocally post-date the scarp formation.

We were able to derive ages using the BCC approach for all the studied scarps (Table 3). In four of the cases, the ages compared well with those we considered to be the best ages derived using the traditional techniques (proximity to scarp, lowest slope available, no suspected local non-scarp geological activity; Table 3). In general, the errors for the BCC ages were larger than for the traditional counts. The larger errors are caused primarily by the smaller numbers of craters available for fitting (see plots for numbers of craters fit), which results from the smaller count area – a line along the scarp trace. The similarity of the ages also generally validates the measurement of craters within a count area defined along the scarp antiform, as done with the more generous buffer definition of Senthil Kumar et al. (2016) for lunar scarps, as well as

Table 3
Previously determined scarp ages from crater degradation age determinations by Binder and Gunga (1985) compared with absolute model ages derived via BCC (cumulative fits) and traditional CSFD measurements (Poisson fits for locations with minimum available slopes at or near the scarps).

Scarp	Crater degradation age (Ma)	BCC AMAs (Ma)	Traditional AMAs (Ma)
Henderson-2	210 ± 60	75 ± 20	77 ± 9
Kondratyuk	680 ± 250	61 ± 20	79 ± 5
Koval'skiy-3	240 ± 60	120 ± 50	160 ± 30
Mandel'shtam-3	180 ± 50	56 ± 8[a]	98 ± 8
Morozov-1	140 ± 50	91 ± 30	84 ± 10

[a] May indicate continued activity on the scarp not recorded on the surrounding surfaces.

by Giacomini et al. (2015) for mercurian scarps. However, in their work on Mercury Giacomini et al. (2015) do note that the ages they derived via the more liberal buffer method are older (within error) than the stringent method, probably because the more liberal method includes some craters that existed prior to the scarp formation.

The primary disadvantage of the BCC approach is that it requires the worker to decide which craters post-date the scarp for inclusion in the measurement, while craters pre-dating the scarp should be excluded. The consequence of excluding craters that post-date the scarp would be that the age determination would be too young. If craters that were present prior to the scarp are included, the derived age will be too old. Determining the relative ages of the craters and scarps can be quite difficult, especially when measuring scarps near the limits of image resolution. Senthil Kumar et al. (2016) also discuss this challenge, commenting that it was also not possible to easily discern the relationships between ejecta blankets that may or may not crosscut the scarps they investigated. Wichman and Schultz (1989) also caution against including crater ejecta in the measurements, because ejecta may not clearly exhibit features that allow the determination of superposition relationships. The inclusion of crosscutting ejecta blankets is a strategy for improving the data set that works well in some cases (Fassett and Head, 2008; Giacomini et al., 2015; Kneissl et al., 2015). However, both Senthil Kumar et al. (2016) and we decided to only measure crosscutting craters, but not ejecta, because we found it to be difficult to discern whether crater ejecta crosscut the scarps due to the overall small sizes of the craters we measured.

Given that the BCC measurement typically encompasses one entire scarp or scarp complex/group (due to the need to measure as many craters as possible), the resulting age represents the end of the formation of the scarp or the last measureable evidence for movement on the fault(s) (e.g., Kneissl et al., 2015). However, the steep slopes of and surrounding the scarps could be affected by ongoing gravity-driven mass-wasting, erasing and covering small impact craters that postdate the last fault movement resulting in underestimated ages (Titley, 1966; Head, 1975; Platz et al., 2013). Another possible effect that could decrease the AMA determined at scarp faces is the shielding of the surface from a portion of impactors by the steep slopes, which could cause a reduction in impact craters measureable at the foot of the scarp. This effect would also depend on the local and regional slope conditions. Some of these caveats may help explain why two of the BCC AMAs we derived are significantly younger than those we determined using the traditional approach. For example, at Mandel'shtam we may have either missed post-scarp craters along the scarp trace, or the scarp may have continued to be active, but at a level not significant enough to reset the crater record in the traditional count areas. At Koval'skiy, the diffuse nature of the scarp at high resolution made it difficult to confidently define the fault trace – a step critical to obtaining a good result. When we separated the northern and southern segments, it became apparent that the northern segment was causing the overall age to be significantly reduced (Fig. 8). In this case, either the steep slope in the northern segment caused erasure of craters that should have been included in the measurement, or the very small sample size caused statistical problems with the fitting of an age.

For the traditional measurements, several of the challenges associated with BCC measurements are eliminated. First, all the craters within the traditional count area are measured, without the need to determine whether they pre- or post-date the scarp formation event. Traditional measurements also allow for the definition of larger count areas, which increases the numbers of craters that can be measured and thus decreases the statistical errors on the age determination. Finally, the traditional CSFDs provide additional information about the pre-existing crater populations – for example when the larger crater diameter ranges can be fit with older ages.

4.3. Seismic resetting of the cratering chronology

The similarity between the BCC and traditional ages that we derived for lobate scarps (Table 3) shows that the scarp formation event not only caused the formation of linear tectonic features on the Moon, but also generated enough seismic shaking in the surrounding terrain to reset the cratering chronology. However, could there also be morphological evidence for seismic shaking in our study regions?

Titley (1966) observed morphologies in the Ranger photographs which are consistent with slumping, creep, and differential compaction. The features were not just observed in locations where slope instability could be invoked to explain them, rather also in locations where no apparent instability could be observed. Thus, he concluded that the seismic activity associated with small impacts could cause compaction, slope failure and debris creep, in an analog to the effects of terrestrial earthquakes. Meanwhile, Schultz and Gault (1975) interpreted the hummocky and subdued textures on lunar ejecta blankets to result from seismically generated creep and compaction. They suggest that craters in incompetent material (such as highlands plains and/or regolith layers) would exhibit subdued, funnel-shaped, dimple-floored, or mounded-floored profiles as a result of seismic shaking causing creep and slumping of the walls (Schultz and Gault, 1975). Later, the absence of small craters, as well as the advanced degradation states of craters on the asteroid 433 Eros were also postulated and modeled to result from impact-related seismic shaking (Veverka et al., 2001; Richardson et al., 2004, 2005).

The areas surrounding the scarps we investigated also show morphological evidence for slumping due to inherent slope instability on the somewhat steep regional slopes along large crater walls. For example, the regional slopes at Henderson-2 (Figs. 1b and 3) and Kondratyuk (Fig. 5) likely cause the footwalls in both cases to exhibit hummocky textures, with craters that have asymmetrical down-slope oriented degradation features. This mass

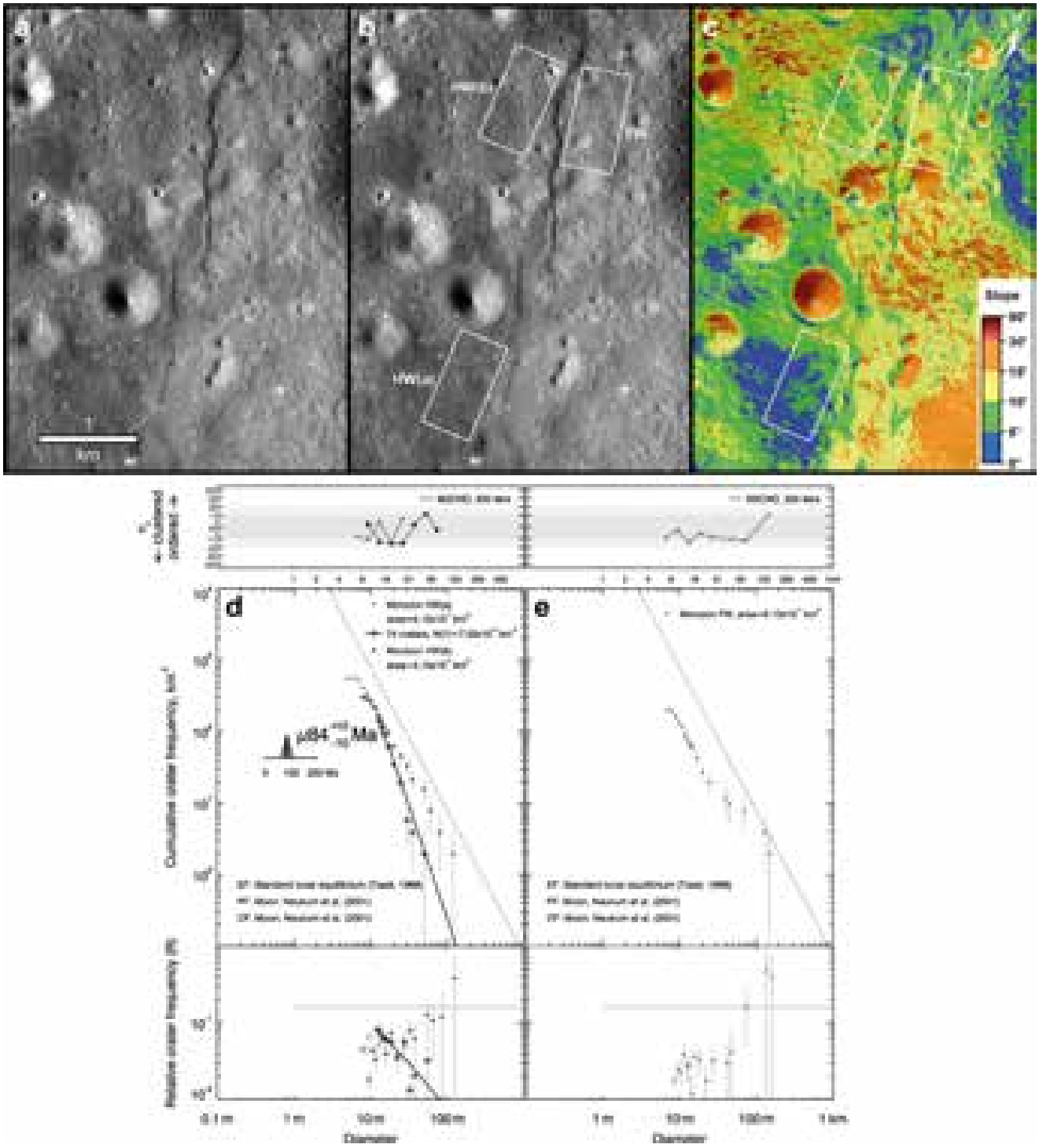

Fig. 12. Morozov scarp (a) NAC frame M1113318442, (b) count area locations, where HW = hanging walls and FW = footwall, and (c) NAC DTM-derived slope map. (d,e) Cumulative and relative crater frequency plots showing AMAs determined using Poisson timing analysis, where applicable. (d) HW(a), gives an age of ~84 Ma, whereas HW(b) is in equilibrium and cannot be fit with an AMA. (e) The CSFD of the footwall cannot be fit with an AMA because it does not conform to the lunar production function.

wasting is probably also enhanced by additional seismic shaking. However, highly degraded, very shallow craters, with v-shaped forms are encountered on relatively flat surfaces, for example at Mandel'shtam-3 (Fig. 1a) and at Koval'skiy (Fig. 7). These degraded craters are almost always the largest craters in the studied regions. For example, at the Mandel'shtam-3 count area HWP(b) (Fig. 9d,e), craters larger than 50 m in diameter exhibit v-shaped profiles, while the craters < 20 m in diameter exhibit typical bowl-shaped forms and are much easier to measure, given their morphologic freshness. For craters with diameters of 20–50 m, there is a mixture of crisp, fresh morphologies and highly degraded, shallow, v-shaped craters.

The diameter dependency of the morphological features is directly reflected in the traditional CSFD plots and fits we made. The diameter range of the smaller, fresher craters represent the fit range for the young AMAs we interpret to represent a scarp for-

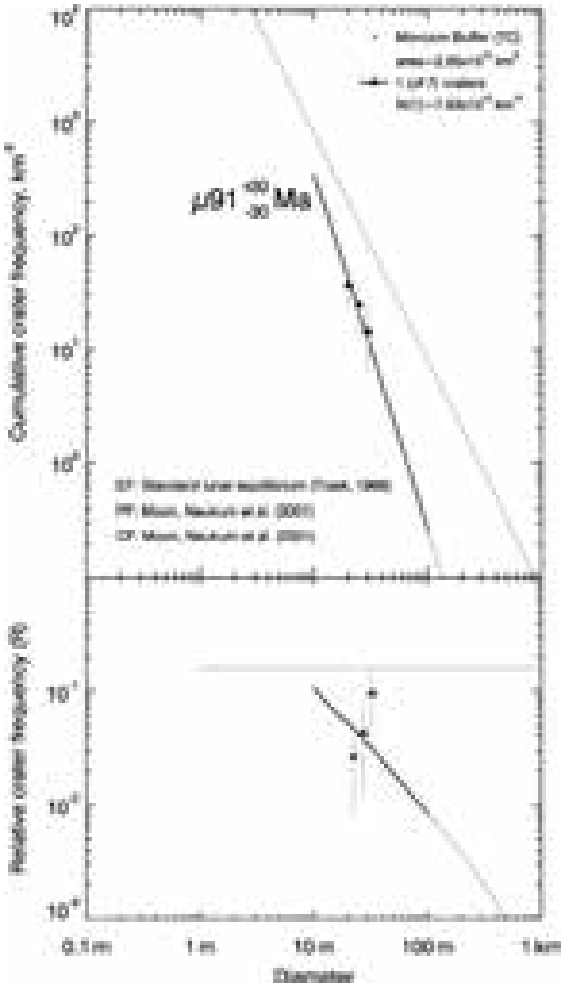

Fig. 13. The AMA derived for Morozov-1 and Morozov-2 together via buffered CSFD measurements (cumulative fit) using the SELENE Terrain Camera orthomap is similar to the HW(b) result. As a stand-alone measurement, this result is not robust due to the small number of data points and the poor fit in the R-plot.

mation or reactivation age. The larger more degraded craters give older AMAs that may be either indicative of earlier more severe or possibly extended scarp activity, or of the background age of the underlying geological unit (e.g., highlands materials or impact ejecta). In cases where the surface is in equilibrium, such as at Morozov (Fig. 12) and some parts of Mandel'shtam (Fig. 10d, area HWD(a)), this could indicate that the ground motion was not significant enough to reset the crater chronometer.

The more detailed study at Mandel'shtam illustrates that scarp-related seismicity affected regions even ~3 km distant from the scarp. The variability in the intensity of the ground motion may be recorded by the largest crater diameter reset during the event; these values are reflected by the fit ranges selected for the AMAs (Table 2). For example, HWP(c) contains craters up to 100 m in diameter that were reset by the event, whereas HWP(a) only exhibits resetting for craters up to 22 m in diameter. This suggests that ground motion at HWP(c) was stronger and/or of a longer duration than at HWP(a) in order to erase the larger craters. Area HWP(b) shows effects for craters < 38 m in diameter. Thus, local variations in the degree of seismic shaking can cause variations in the level to which the crater population is affected. So, the variations in the CSFD around a scarp yield information about the intensity and spatial extent of seismic shaking involved in the cumulative coseismic slip events that formed the scarps.

4.4. How old are lunar lobate scarps?

Binder and Gunga (1985) concluded that lunar scarps are Copernican in age, with ages ranging from 60 ± 30 to 680 ± 250 Ma. In their analyses, they noted that scarps fell into two different groups based on their age characteristics: (1) scarp complexes or groups with a unique age – most ages derived for scarp complexes indicated a coeval formation of the segments (e.g., Mandel'shtam with ages of 100 ± 70 to 190 ± 70 Ma), and (2) scarp complexes with distinctly different ages between their subscarps (e.g., Koval'skiy with ages of 240 ± 60 and 620 ± 280 Ma). These crater degradation ages were argued to be biased to older ages due to limitations on the technique: (1) the resolution (~2 m) of the panoramic imagery results in the softening of rims of small (10–40 m diameter) craters therefore making them appear larger and older, and (2) the method of Trask (1971) for assessing crater degradation age was created for craters on flat mare surfaces, rather than hilly highlands areas (Binder and Gunga, 1985). The latter concern could cause the age estimates to be older than actual, because highlands materials may degrade quicker than mare materials due to their physical properties, although the differences between the degradation rates are not yet clear (Mahanti et al., 2017, 2018; van der Bogert et al., 2017). In addition, the slope maps we used in our study show that some of the studied scarps exhibit significant slopes, which may have caused some of the craters measured by Binder and Gunga (1985) to have experienced enhanced slope-related degradation – resulting in older than actual age estimates.

Watters et al. (2010) estimated the ages of scarps to also be Copernican based on the fact that many scarps are crosscut by craters < 50 m in diameter. Craters < 50 m in diameter are, based on their expected degradation lifetime, Copernican (< 800 ± 15 Ma) in age (Trask, 1971). Watters et al. (2012; 2015) argued that small-scale graben associated with some scarps must also be extremely young since they would be expected to fill in and disappear quickly. For example, with a fill rate of 5 ± 3 cm/Ma, based on boulder track erasure (Arvidson et al., 1975), a graben with ~1 m depth would be expected to fill in ~12.5–50 Ma. A young age for associated flexural features would necessitate a young age for the primary scarp itself. In fact, Watters et al., (2015, 2017) suggest that the young fault activity may be associated with recent shallow moonquakes, of which 28 were recorded by Apollo instrumentation (Nakamura et al., 1979; Watters and Johnson, 2010).

The ages that we derived from CSFDs at and around the five study scarps (Tables 2 and 3) also support a late Copernican age, approaching the young ages estimated by Watters et al. (2012; 2015), and consistent with the ages determined by Senthil Kumar et al. (2016) for four scarps in the Schrödinger basin (11–85Ma). At Henderson-2, Kondratyuk, Koval'skiy-3, and Morozov, our BCC and traditional AMAs are similar to one another, suggesting that these areas reflect a short period of tectonic activity that reset the surrounding crater record, while forming the scarp. However, the younger BCC versus traditional AMAs derived for Mandel'shtam might suggest that minor scarp movement continued after a more significant shaking event that was recorded in the surrounding terrain, or that we were only able to obtain an incomplete count due to similar challenges as encountered at Koval'skiy-3.

By using LROC NAC images with pixel scales approaching 1 m/pixel, we were able to measure the diameters of smaller craters than Binder and Gunga (1985) were able to identify on the Apollo panoramic images. Having measured a population of craters with CSFD techniques, rather than investigating the degradation states of individual craters, we also have a de facto test of consistency of the crater diameter measurements (via the wellness of the fit with the lunar production function) down to the limit of the current chronology function at 10 m crater diameters. Thus,

it is not surprising that our AMAs provide younger, more precise estimates than the study of Binder and Gunga (1985). One caveat of the traditional approach, however, is that the diameters of the craters affected by seismic shaking and degradation may be larger than expected for the pre-scarp population of craters, leading to an overestimation of these surface ages. Nevertheless, our data illustrate that focused studies using different CSFD techniques at individual scarps can and do shed light on their detailed tectonic histories (e.g., Mandel'shtam, Clark et al., 2016).

5. Conclusions

The late-Copernican ages we derived via both buffered and traditional crater size-frequency distribution measurement techniques are younger than age determinations based on crater degradation measurements (Binder and Gunga, 1985), and slightly older than ages estimated from the expected life-times of the scarps and their associated small graben (Watters et al., 2010, 2012, 2015). The similarity between BCC and traditional CSFD measurements at and around many of the lunar scarps we studied indicates that scarp-related seismicity reset the crater chronometer not only at, but also in the terrain surrounding lobate scarps. This observation suggests that shallow moonquakes may be associated with tectonic activity at lunar scarps. Further studies are needed to explore the magnitudes and extents of shaking around scarps and to evaluate how this may relate to scarp morphology and topology. Global assessment of scarp formation ages could provide information about the overall tectonic evolution of the Moon (Clark et al., 2017a).

Acknowledgments

C. H. vdB., J. D. C., and H. H. were funded by German Aerospace Center (Deutsches Zentrum für Luft- und Raumfahrt) projects 50OW0901 (via the BMBF - Bundesministerium für Bildung und Forschung) and 50OW1504 (via the BMWi - Bundesministerium für Wirtschaft und Energie). MEB and TRW were supported by the LRO Project and NASA grant NNX08AM73G. We gratefully acknowledge the Lunar Reconnaissance Orbiter (LRO) and Lunar Reconnaissance Orbiter Camera (LROC) engineers and technical support personnel. Special thanks go to Megan Henriksen, Madeleine Manheim, and the LROC SOC team for generating the NAC DTMs used in this study. We thank the reviewers, Amanda Nahm and Matteo Massironi, for their helpful comments and suggestions.

References

Anderson, J.A., Sides, S.C., Soltesz, D.L., Sucharski, T.L., Becker, K.J., 2004. Modernization of the integrated software for imagers and spectrometers. In: 35th Lunar and Planetary Science Conference, p. 2039.

Arvidson, R, Drozd, R.J., Hohenberg, C.M., Morgan, C.J., Poupeau, G., 1975. Horizontal transport of the regolith, modification of features, and erosion rates on the lunar surface. The Moon 13, 67–79.

Banks, M.E, Watters, T.R., Robinson, M.S., Tornabene, L.L., Tran, T., Ojha, L., Williams, N.R., 2012. Morphometric analysis of small-scale lobate scarps on the Moon using data from the Lunar Reconnaissance Orbiter. J. Geophys. Res. 117, E00H11. doi:10.1029/2011JE003907.

Banks, M.E, Watters, T.R., Strom, R.G., Braden, S.E., Chapman, C.R., Solomon, S.C., Klimczak, C., Byrne, P.K., 2015. Duration of activity on lobate-scarp thrust faults on Mercury. J. Geophys. Res. Planet 120, 1751–1762.

Barker, M.K., Mazarico, E., Neumann, G.A., Zuber, M.T., Haruyama, J., Smith, D.E., 2016. A new lunar digital elevation model from the Lunar Orbiter Laser Altimeter and SELENE Terrain Camera. Icarus 273, 346–355.

Basilevsky, A.T., 1976. On the evolution rate of small lunar craters. In: Proceedings of the 7th Lunar Science Conference, pp. 1005–1020.

Basilesky, A.T., Head, J.W., Fassett, C.I., Michael, G., 2011. History of tectonic deformation in the interior plains of the Caloris basin, Mercury. Sol. Syst. Res. 45, 471–497.

Binder, A.B., Gunga, H.C., 1985. Young thrust-fault scarps in the highlands: evidence for an initially totally molten moon. Icarus 63, 421–441.

Boyce J.M. and Moore H.J., 1980, Ages of Lunar Plains in Lunar Remote Sensing and Measurements (Apollo 15-17 Orbital Investigations), Moore H. J., Boyce J. M., Schaber G. G., and Scott D. H., eds., U.S. Geological Survey Professional Paper 1046-B, B3–B18, https://pubs.usgs.gov/pp/1046b/report.pdf.

Clark, J.D., Hurtado Jr., J.M., Hiesinger, H., Bernhardt, H., van der Bogert, C.H., 2017a. Investigation of lobate scarps: Implications for the tectonic and thermal evolution of the Moon. Icarus 298, 78–88.

Clark, J.D., van der Bogert, C.H., Hiesinger, H., 2016. An in-depth investigation of the Mandel'shtam lobate scarp complex. In: 47th Lunar and Planetary Science Conference, p. 2956.

Clark, J.D., van der Bogert, C.H., Hiesinger, H., Bernhardt, H., 2017b. Wrinkle ridge-lobate scarp transition of West Serenitatis: indications for recent tectonic activity. In: 48th Lunar and Planetary Science Conference, p. 1001.

Crater Analysis Techniques Working Group, 1979. Standard techniques for presentation and analysis of crater size-frequency data. Icarus 37, 467–474.

Fassett, C.I., Head, J.W., 2008. The timing of martian valley network activity: constraints from buffered crater counting. Icarus 195, 61–89.

Fegan, E.R., Rothery, D.A., Marchi, S., Massironi, M., Conway, S.J., Anand, M., 2017. Late movement of basin-edge lobate scarps on Mercury. Icarus 288, 226–234.

Giacomini, L., Massironi, M., Marchi, S., Fassett, C.I., Di Achille, G., Cremonese, G., 2015. Age dating of an extensive thrust system on Mercury: Implications for the planet's thermal evolution. In: Platz, T., Massironi, M., Byrne, P.K., Hiesinger, H. (Eds.). In: Volcanism and Tectonism Across the Inner Solar System, 401. Geological Society, London, pp. 291–311. Special Publications.

Hartmann, W.K., 1966. Early lunar cratering. Icarus 5, 406–418.

Haruyama, J., Matsunaga, T., Ohtake, M., Morota, T., Honda, C., Yokota, Y., Torii, M., Ogawa, Y.the LISM Working Group, 2008. Global lunar-surface mapping experiment using the Lunar Imager/Spectrometer on SELENE. Earth Planets Space 60, 243–255.

Head, J.W., 1975. Processes of lunar crater degradation – Changes in style with geologic time. The Moon 12, 299–329.

Henriksen, M.R., Manheim, M.R., Burns, K.N., Seymour, P., Speyerer, E.J., Deran, A., Boyd, A.K., Howington-Kraus, E., Rosiek, M.R., Archinal, B.A., Robinson, M.S., 2017. Extracting accurate and precise topography from LROC Narrow Angle Camera stereo observations. Icarus 283, 122–137.

Hiesinger, H., Jaumann, R., Neukum, G., Head III., J.W., 2000. Ages of mare basalts on the lunar nearside. J. Geophys. Res. 105, 29239–29275.

Hiesinger, H., Head, IIIJ.W., Wolf, U., Jaumann, R., Neukum, G., 2011. Ages and Stratigraphy of Lunar Mare Basalts: A Synthesis. Geological Society of America, pp. 1–51. Special Paper 477.

Kneissl, T., van Gasselt, S., Neukum, G, 2011. Map-projection-independent crater size-frequency determination in GIS environments – New software tool for ArcGIS. Planet. Space Sci. 59, 1243–1254.

Kneissl, T., Michael, G.G., Platz, T., Walter, S.H.G., 2015. Age determination of linear surface features using buffered crater counting approach – Case studies of the Sirenum and Fortuna Fossae graben systems on Mars. Icarus 250, 384–394.

Le Feuvre, M., Wieczorek, M.A., 2011. Nonuniform cratering of the Moon and a revised crater chronology of the inner Solar System. Icarus 214, 1–20.

Lucchitta, B.K., 1976. Mare ridges and related highland scarps – Result of vertical tectonism? In: Proceedings of the 7th Lunar and Planetary Science Conference, pp. 2761–2782.

Mahanti, P., Robinson, M.S., Thompson, T.J., Henriksen, M.R., 2018. Small lunar craters at the Apollo 16 and 17 landing sites – Morphology and degradation. Icarus 299, 475–501.

Mahanti, P., Robinson, M.S., Thompson, T.J., van der Bogert, C.H., 2017. Small crater degradation at the Apollo landing sites – Characterizing differences in degradation rates. In: 48th Lunar and Planetary Science Conference, p. 2089.

Meyer, H.M., Mahanti, P., Robinson, M.S., Boyd, A., 2016. Quantifying the effect of slope on age estimates: a preliminary overview. In: 47th Lunar and Planetary Science Conference, p. 2740.

Michael, G.G., 2013. Planetary surface dating from crater size-frequency distribution measurements: multiple resurfacing episodes and differential isochron fitting. Icarus 226, 885–890.

Michael, G.G., Kneissl, T., Neesemann, A., 2016. Planetary surface dating from crater size-frequency measurements: Poisson timing analysis. Icarus 277, 279–285.

Michael, G.G., Neukum, G., 2010. Planetary surface dating from crater size-frequency distribution measurements: Partial resurfacing events and statistical age uncertainty. Earth Planet. Sci. Lett. 294, 223–229.

Michael, G.G., Platz, T., Kneissl, T., Schmedemann, N., 2012. Planetary surface dating from crater size-frequency distribution measurements: Spatial randomness and clustering. Icarus 218, 169–177.

Moore, H.J., Boyce, J.M., Hahn, D.A., 1980. Small impact craters in the lunar regolith – Their morphologies, relative ages, and rates of formation. Moon Planets 23, 231–252.

Nakamura, Y., Latham, G.V., Dorman, H.J., Ibrahim, A.-B.K., Koyana, J., Horvath, P., 1979. Shallow moonquakes – Depth, distribution, and implications as to the present state of the lunar interior. In: Proceedings of 10th Lunar and Planetary Science Conference, pp. 2299–2309.

Neukum, G., 1983. Meteorite Bombardment and Dating of Planetary Surfaces. Translation of: Meteoritenbombardement und Datierung planetarer Oberflächen, Tenure Thesis, NASA Technical Memorandum TM-77558. Ludwig-Maximilians University, Munich, Germany, p. 153.

Neukum, G., Ivanov, B.A., 1994. Crater size distributions and impact probabilities on Earth from lunar, terrestrial-planet, and asteroid cratering data. In: Gehrels, T. (Ed.), Hazard Due to Comets and Asteroids. University of Arizona Press, Tucson, Arizona, pp. 359–416.

Neukum, G., Ivanov, B.A., Hartmann, W.K., 2001. Cratering records in the inner solar system in relation to the lunar reference system. Space Sci. Rev. 96, 55–86.

Offield T.W. and Pohn H.A., 1970, Lunar Crater Morphology and Relative-Age Determination of Lunar Geologic Units – Part 2. Applications, U.S. Geological Survey Professional Paper 700-C, C163–C169, https://pubs.er.usgs.gov/publication/pp700C.

Ostrach, L.R., Robinson, M.S., Denevi, B.W., Thomas, P.C., 2011. Effects of incidence angle on crater counting observations. In: 42nd Lunar and Planetary Science Conference, p. #1202.

Pasckert, J.H., Hiesinger, H., van der Bogert, C.H., 2015. Small-scale lunar farside volcanism. Icarus 257, 336–354.

Platz, T., Michael, G., Tanaka, K.L., Skinner, J.A., Fortezzo, C.M., 2013. Crater-based dating of geological units on Mars: Methods and applications for the new global geological map. Icarus 225, 806–827.

Pohn H.A. and Offield T.W., 1970, Lunar Crater Morphology and Relative-Age Determination of Lunar Geologic Units – Part 1. Classification, U.S. Geological Survey Professional Paper 700-C, C153–C162, https://pubs.er.usgs.gov/publication/pp700C.

Richardson Jr., J.E., Melosh, H.J., Greenberg, R.J., 2004. Impact-induced seismic activity on Asteroid 433 Eros: A surface modification process. Science 306, 1526–1529.

Richardson Jr., J.E., Melosh, H.J., Greenberg, R.J., O'Brien, D.P., 2005. The global effects of impact-induced seismic activity on fractured asteroid surface morphology. Icarus 179, 325–349.

Robinson, M.S., Brylow, S.M., Tschimmel, M., Humm, D., Lawrence, S.J., Thomas, P.C., Denevi, B.W., Bowman-Cisneros, E., Zerr, J., Ravine, M.A., Caplinger, M.A., Ghaemi, F.T., Schaffner, J.A., Malin, M.C., Mahanti, P., Bartels, A., Anderson, J., Tran, T.N., Eliason, E.M., McEwen, A.S., Turtle, E., Jolliff, B.L., Hiesinger, H., 2010. Lunar Reconnaissance Orbiter Camera (LROC) instrument overview. Space Sci. Rev. 150, 81–124.

Roggon, L., Hetzel, R., Hiesinger, H., Clark, J.D., Hampel, A., van der Bogert, C.H., 2017. Length-displacement scaling of thrust faults on the Moon and the formation of uphill-facing scarps. Icarus 292, 111–124.

Schultz, P.H., 1976. Moon Morphology: Interpretations Based on Lunar Orbiter Photography. University of Texas Press, Austin, Texas, p. 626.

Schultz, P.H., Gault, D.E., 1975. Seismically induced modification of lunar surface features. In: Proceedings of the 6th Lunar Science Conference, pp. 2845–2862.

Schultz, P.H., Gault, D., Greeley, R., 1977. Interpreting statistics of small lunar craters. In: Proceedings of the 8th Lunar Science Conference, pp. 3539–3564.

Senthil Kumar, P., Sruthi, U., Lakshmi, K.J.P., Menon, R., Amitabh, KrishnaB.G., Kring, D.A., Head, J.W., Goswami, J.N., Kumar, A.S.K., 2016. Recent shallow moonquakes and impact-triggered boulder falls on the Moon: New insights from the Schrödinger basin. J. Geophys. Res. 121, 147–197.

Soderblom, L.A., 1970. A model for small-impact erosion applied to the lunar surface. J. Geophys. Res. 75, 2655–2661.

Stöffler, D., Ryder, G., 2001. Stratigraphy and isotope ages of lunar geologic units: chronological standard for the inner solar system. Space Sci. Rev. 96, 9–54.

Stöffler, D., Ryder, G., Ivanov, B.A., Artemieva, N.A., Cintala, M.J., Grieve, R.A.F., 2006. Cratering history and lunar chronology. In: Jolliff, B.L., Wieczorek, M.A., Shearer, C.K., Neal, C.R. (Eds.). In: New Views of the Moon, 60. Mineralogical Society of America, pp. 519–596. *Rev. Min. Geochem.*.

Tanaka K.L., 1982, A New Time-Saving Crater-Count Technique, with Application to Narrow Features, NASA *Technical Memorandum TM-85127*, 123–125.

Titley, S.R., 1966. Seismic energy as an agent of morphologic modification on the Moon. In: Astrogeologic Studies, Annual Progress Report Part A Lunar and Planetary Investigations. U. S. Geological Survey, pp. 87–103. NASA-CR-86649.

Tran, T., Rosiek, M.R., Beyer, R.A., Mattson, S., Howington-Kraus, E., Robinson, M.S., Archinal, B.A., Edmundson, K., Harbour, D., Anderson, E.the LROC Science Team, 2010. Generating digital terrain models using LROC NAC images. ASPRS/CaGIS 2010 Fall Special Conference http://www.isprs.org/proceedings/XXXVIII/part4/files/Tran.pdf.

Trask, N.J., 1966. Size and Spatial Distribution of Craters Estimated from the Ranger Photographs in Ranger VIII and IX, Part II, Experimenters' Analyses and Interpretations. California Institute of Technology, Jet Propulsion Lab., pp. 252–264. *Technical Report* 32-800.

Trask N.J., 1971, Geologic Comparison of Mare Materials in the Lunar Equatorial Belt, Including Apollo 11 and Apollo 12 Landing Sites, U.S. Geological Survey Professional Paper 750-D, D138–D144, https://pubs.usgs.gov/pp/0750d/report.pdf

van der Bogert, C.H., Hiesinger, H., Dundas, C., Krüger, T., McEwen, A.S., Zanetti, M., Robinson, M.S., 2017. Origin of discrepancies between crater size-frequency distributions of coeval lunar geologic units via target property contrasts. Icarus 298, 49–63.

van der Bogert, C.H., Michael, G., Kneissl, T., Hiesinger, H., Pasckert, J.H., 2015. Effects of count area size on absolute model ages derived from random crater size-frequency distributions. In: 46th Lunar Science Conference #1742.

Veverka, J., Thomas, P.C., Robinson, M.S., Murchie, S., Chapman, C., Bell, M., Harch, A., Merline, W.J., Bell III, J.F., Bussey, B., Carcich, B., Cheng, A., Clark, B., Domingue, D., Dunham, D., Farquar, R., Gaffey, M.J., Hawkins, E., Izenberg, N., Joseph, J., Kirk, R., Li, H., Lucey, P., Malin, M., McFadden, L., Miller, J.K., Owen Jr., W.M., Peterson, C., Prockter, L., Warren, J., Wellnitz, D., Williams, B.G., Yeomans, D.K., 2001. Imaging of small-scale features on 433 Eros from NEAR: Evidence for a complex regolith. Science 292, 484–488.

Watters, T.R., Daud, K., Banks, M.E., Selvans, M.M., Chapman, C.R., Ernst, C.M., 2016. Recent tectonic activity on Mercury revealed by small thrust fault scarps. Nat. Geosci. 9, 743–747.

Watters, T.R., Johnson, C.L., 2010. Lunar tectonics. In: Watters, T.R., Schultz, R.A. (Eds.), Planetary Tectonics. Cambridge University Press, New York, pp. 121–182.

Watters, T.R., Robinson, M.S., Beyer, R.A., Banks, M.E., Bell, J.F., Pritchard, M.E., Hiesinger, H., van der Bogert, C.H., Thomas, P.C., Turtle, E., Williams, N.R., 2010. Evidence of recent thrust faulting on the Moon revealed by the Lunar Reconnaissance Orbiter Camera. Science 329 (5994), 936–940.

Watters, T.R., Robinson, M.S., Banks, M.E., Tran, T., Denevi, B.W., 2012. Recent extensional tectonics on the Moon revealed by the Lunar Reconnaissance Orbiter Camera. Nat. Geosci. 5, 181–185.

Watters, T.R., Robinson, M.S., Collins, G.C., Banks, M.E., Daud, K., Williams, N.R., Selvans, M.M., 2015. Global thrust faulting on the Moon and the influence of tidal stresses. Geology 43, 851–854.

Watters, T.R., Weber, R.C., Collins, G.C., Johnson, C.L., 2017. Shallow lunar seismic activity and the current stress state of the Moon. In: 48th Lunar Science Conference #2569.

Wichman, R.W., Schultz, P.H., 1989. Sequence and mechanisms of deformation around the Hellas and Isidis impact basins on Mars. J. Geophys. Res. 94, 17333–17357.

Wilcox, B.B., Robinson, M.S., Thomas, P.C., Hawke, B.R., 2005. Constraints on the depth and variability of the lunar regolith. Meteorit. Planet. Sci. 40, 695–710.

Williams, J.-P., van der Bogert, C.H., Pathare, A.V., Michael, G.G., Kirchoff, M.R., Hiesinger, H., 2017. Dating very young planetary surfaces from crater statistics: a review of issues and challenges. Meteorit. Planet. Sci. doi:10.1111/maps.12924.

Williams, N.R., Watters, T.R., Pritchard, M.E., Banks, M.E., Bell, J.F., 2013. Fault dislocation modeled structure of lobate scarps from Lunar Reconnaissance Orbiter Camera Digital Terrain Models. J. Geophys. Res. 118, 224–233.

Young, R.A., 1975. Mare crater size-frequency distributions: implications for relative surface ages and regolith development. Proc. Lunar Sci. Conf. 6, 2645–2662.